



Bayesian retinex underwater image enhancement

Peixian Zhuang ^{a,*}, Chongyi Li ^b, Jiamin Wu ^a

^a Department of Automation, Tsinghua University, Beijing, China

^b School of Computer Science and Engineering, Nanyang Technological University, Singapore



ARTICLE INFO

Keywords:

Underwater image enhancement
Retinex decomposition
Multiorder gradients
Maximum a posteriori
Alternative optimization

ABSTRACT

This paper develops a Bayesian retinex algorithm for enhancing single underwater image with multiorder gradient priors of reflectance and illumination. First, a simple yet effective color correction approach is adopted to remove color casts and recover naturalness. Then a maximum a posteriori formulation for underwater image enhancement is established on the color-corrected image by imposing multiorder gradient priors on reflectance and illumination. The l_1 norm is appropriately used to model piecewise and piecewise linear approximations on the reflectance, and the l_2 norm is used to enforce spatial smoothness and spatial linear smoothness on the illumination. Meanwhile, a complex underwater image enhancement issue is turned into two simple denoising subproblems where their convergence analyses are mathematically provided, and their solutions can be derived by an efficient optimization algorithm. Besides, the proposed model is fast implemented on pixelwise operations while not requiring additional prior knowledge about underwater imaging conditions. Final experiments demonstrate the effectiveness of the proposed method in color correction, naturalness preservation, structures and details promotion, artifacts or noise suppression. Compared with several traditional and leading enhancement approaches, the proposed method yields better results on qualitative and quantitative assessments. The superiority of the proposed method can be extended to several challenging applications.

1. Introduction

Since abundant resources are contained in oceans, rivers and lakes, underwater imaging has been an important and valuable research field that receives much attention for a few decades (Raimondo and Silvia, 2010). Unlike natural image processing, underwater image processing is more challenging due to complicated physical properties of underwater environment, and underwater images easily suffer from color distortion and contrast degradation generated from the absorption and scattering when light is traveling in water. A schematic diagram of underwater optical imaging model is shown in Fig. 1(a) where the light captured by the camera is mainly constituted by three components: the direct component (light reflected from the object that has not been scattered in water), the forward scattering component (light reflected from the object that has been scattered at small angles), and the backward scattering component (light reflected not from the target object but from floating particles). An underwater image can be viewed as a linear superposition of the three components. However, the forward scattering component leads to the blurred structures of underwater images whereas the backward scattering component veils underwater image edges and details. Meanwhile, color distortion of underwater images usually results from absorption of different wavelengths at different rates. As can be seen in Fig. 1(b), different wavelengths of light are attenuated at different rates, concretely, the red light disappears

firstly in the water since it has longest wavelength or minimum energy, whereas the blue or green light shows the opposite case (Li et al., 2020; Ancuti et al., 2012). This property makes captured underwater images appear bluish or greenish. The absorption enormously reduces light energy while the scattering case haphazardly changes light propagation direction, and these underwater properties eventually produce underwater images of both color shift and contrast degradation, which are urgently desired to yield high quality underwater images for subsequent processing. In order to address the issues of color distortion and contrast degradation, a Bayesian retinex algorithm with multiorder gradient priors of both reflectance and illumination is proposed for enhancing single underwater image. The main contributions of this paper are summarized below:

- A simple but effective color correction method is employed to address the color distortion of underwater images, and this correction can yield better color restoration and more visually-satisfied naturalness preservation than widely-used color constancy approaches.
- From the viewpoint of Bayesian modeling, a maximum a posteriori (MAP) formulation for retinex underwater image enhancement is established with multiorder gradient priors on the above color-corrected image, where first-order and second-order gradient priors are imposed on both reflectance and illumination to

* Corresponding author.

E-mail address: zhuangpeixian0624@163.com (P. Zhuang).

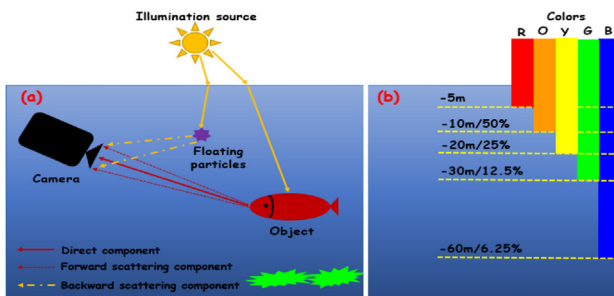


Fig. 1. Schematic diagrams of underwater imaging model (a) and light absorption (b). The three components of underwater optical imaging are direct component (red solid line), forward scattering component (red dashed line) and backward scattering component (pale yellow dash-dot line). In water, different wavelengths of light are attenuated at different rates, the red light first disappears due to its longest wavelength (or minimum energy) while the blue or green light travels longer duration due to its shorter wavelength (or larger energy).

capture more fine-scale and complete structures from underwater images. The l_1 norm is effectively used to model piecewise constant and linear approximations on the reflectance since the reflectance is found to be more sparse than the illumination. The l_2 norm is appropriately used to enforce spatial smoothness and linear smoothness on the illumination since the illumination is observed to be relative smoother than the reflectance.

- A complex underwater image enhancement issue is turned into two simple denoising subproblems, and their convergences are mathematically proved and analyzed. Then an efficient alternating optimization method is derived to address the two decomposed subproblems by using shrinkage thresholding, fast Fourier transform (FFT) (Ng and Wang, 2011; Xu and Jia, 2010) and alternating direction method of multipliers (ADMM) (Boyd et al., 2011; Goldstein and Osher, 2009), which can be fast implemented on pixel-wise operations without requiring additional prior knowledge about underwater imaging environment.
- A large number of experiments are provided to demonstrate the effectiveness of the proposed method in terms of color correction and naturalness preservation, structures and details promotion, and artifacts or noise suppression. Compared with several traditional and state-of-the-art underwater image enhancement approaches, the proposed method yields better or comparable results of both subjective visibility and objective assessments. Additionally, a variety of challenging applications, including underwater keypoint detection, underwater saliency detection, underwater depth map estimation, underwater image segmentation, are performed to show the superiority of the proposed method.

The paper is organized below. In Section 2, the related work of underwater image enhancement is reviewed concisely. The proposed retinex underwater enhancement model for simultaneously estimating reflectance and illumination, and its convergence analysis and efficient optimization strategy are detailed in Section 3. Then numerous experiments are provided to demonstrate the effectiveness of the proposed method in Section 4, and concluding remarks are finally presented in Section 5.

2. Related work

In the last few years, numerous underwater restoration and enhancement approaches have emerged to improve the visibility of degraded underwater images, and these existing methods can be divided into three main categories below:

(1) Restoration-based Methods. The first category is based on image restoration-based methods that can recover underwater images

by constructing degradation models. Due to the assumption that underwater images are similar to hazy images to some extents, some dehazing algorithms based on dark channel prior (He et al., 2011) have been employed to enhance degraded underwater images. An underwater optical model (Wen et al., 2013) is proposed to improve the perception of underwater images, and a dark channel prior is used to estimate the scattering rate. A red channel method (Galdran et al., 2015) (ARC) recovers colors associated to short wavelengths for restoring lost contrast. Observing the absorption rate of red channel in abundant underwater images, an underwater dark channel prior (UDCP) (Drews et al., 2016) is presented to restore better underwater results. A depth estimation method based on image blurriness and light absorption (IBLA) (Peng and Cosman, 2017) is proposed to restore underwater images, while previous restoration methods based on dark channel or maximum intensity priors are inaccurate to estimate underwater scene depth. And underwater scene transmission (Peng et al., 2018) is estimated according to depth-dependent color variation, and adaptive color correction is incorporated into an image formation model for restoring color and contrast. In addition, a model combined with wavelength compensation (Chiang and Chen, 2012) is derived to suppress blurring effects of degraded underwater images, and another model of reducing blurring and removing color cast (Farhadifard et al., 2015) is described where a pair of learned dictionaries based on sparse representation are used to sharpen image details. These restoration-based methods are sensitive to model assumptions and exhibit poor enhanced performance in extreme underwater environment, and they are inflexibly implemented since physical parameters and underwater optical property are required.

(2) Enhancement-based Methods. The second category is image enhancement-based methods, which can generate visually appealing underwater images by adjusting image pixel values without requiring physical models. Contrast limited adaptive histogram equalization (CLAHE) (Hitam et al., 2013) is used to enhance image contrast of small region, and the histogram of output region approximately matches the specified histogram. A slide stretching approach (Iqbal et al., 2007) utilizes contrast stretching of RGB to equalize color contrast, and then uses saturation and intensity stretching of HSI to increase color. For the mode of multiple underwater images enhancement, an approach requiring polarization images of different degrees (Schechner and Averbuch, 2007) and another method using multiple images (Narasimhan and Nayar, 2003) are proposed to improve the visibility of underwater images, but the problem inevitably emerges where multiple images cannot be available in practical applications. To address this issue, a fusion-based approach (Ancuti et al., 2012) is developed to blend different filters on a single input, and then a fusion strategy (Fang et al., 2013) is used to apply white balance and global contrast techniques to enhance raw images. Another fusion approach (Ancuti et al., 2018) is introduced for contrast and color promotion, which blends two latent images derived from color-compensated and white-balanced versions of degraded images. In addition, a retinex-based variational framework (Fu et al., 2014) (RBE) is presented to enhance single underwater image, where the reflectance and the illumination are respectively enhanced with different regularizations. A two-step algorithm (Fu et al., 2017) (TSE) introduces a color correction scheme of piecewise linear transformation to restore color, and then an optimal contrast improvement method is utilized to promote contrast. These enhancement-based methods are hard to maintain better consistency between subjective and objective enhancements without imaging process and prior knowledge, and some over-enhanced results may appear in enhanced images.

(3) Deep Learning-based Methods. Based on powerful computation and abundant training data, deep learning (LeCun et al., 2015) achieves convincing success on low-level vision tasks, such as image dehazing (Cai et al., 2016), super-resolution (Dong et al., 2015) and reconstruction (Liu et al., 2018). Meanwhile, great progresses of engineering applications have been made by other deep learning-based and

artificial neural network techniques in Tran-Ngoc et al. (2019), Khatir et al. (2019a), Nguyen et al. (2019), Wang et al. (2021). Deep learning-based methods are capable of improving underwater image quality in different scenes. For color correction of monocular underwater images, WaterGAN (Li et al., 2018b) combines with the physical model and uses the generative adversarial network (GAN) (Goodfellow et al., 2014) to generate synthetic underwater images from in-air image and corresponding depth pairings for specific underwater scenarios. A weakly supervised underwater color transfer model (WSCT) (Li et al., 2018a) is introduced to correct color distortion by relaxing the requirement of paired underwater images for training and allowing for underwater images taken in unknown locations, and based on the cycle-consistent adversarial network (CycleGAN) (Zhu et al., 2012), a multiterm loss function is designed to ensure the consistency of outputs and inputs. In addition, an underwater GAN (UGAN) (Fabbri et al., 2018) employs the CycleGAN to simulate a degradation process to generate paired training data, and then the model based on pix2pix (Isola et al., 2017) is used to improve underwater image quality. These deep learning-based methods demand a large amount of training underwater images and have a long training time.

Uniqueness of Proposed Model. Compared with previous color correction schemes, the proposed method is more capable of alleviating underwater color cast and loss, and is simple but effective in both color correction and naturalness preservation. Different from the aforementioned approaches and the edge-preserving filtering retinex method (Zhuang and Ding, 2020) where gradient domain guided image filtering (GGF) is used in a retinex variational framework, the proposed method is a Bayesian probability model established for underwater image enhancement, and a maximum a posteriori (MAP) for the proposed retinex underwater enhancement model is established with using first-order and second-order gradient priors on the reflectance and the illumination simultaneously. To the best of our knowledge, multiorder gradient priors are adopted in the first time to enhance reflectance and illumination. Unlike the retinex-based model (Fu et al., 2014) using the first-order gradient prior on reflectance and the edge-preserving filtering retinex model (Zhuang and Ding, 2020) using the GGF priors on first-order gradient errors on reflection and illumination, the proposed multiorder gradient priors can capture more fine-scale and complete structures by modeling piecewise constant and linear approximations on the reflectance. Meanwhile, the proposed priors can enforce more appropriate spatial smoothness and spatial linear smoothness on the illumination, which is different from Fu et al. (2014) that only focuses on spatial smoothness of the illumination. And different norms are appropriately employed according to different characteristics of reflectance and illumination, the l_1 norm is used on the reflectance since it is more sparse than the illumination, while the l_2 norm is utilized on the illumination which is relative smoother than the reflectance. It is worth noting that the proposed form of norm constraint is different from Zhuang and Ding (2020) that imposes the l_2 norm on the GGF priors. Moreover, an underwater image enhancement problem, intricately solved by previous enhancement approaches, is transformed into two simple denoising subproblems, and their convergence analyses are mathematically provided, contrary to Fu et al. (2014) where no relevant proof of convergence is given. Then an alternating optimization method is derived to efficiently solve these subproblems using shrinkage thresholding, fast Fourier transform (FFT) and alternating direction method of multipliers (ADMM), which can be rapidly performed on most of the pixel-wise operations. Compared with existing techniques (Schechner and Averbach, 2007; Narasimhan and Nayar, 2003) using multiple underwater images, the proposed method is fast implemented on a single underwater image without requiring complex information about underwater imaging scenes. And the proposed method can yield decent underwater enhancement results in a single-resolution fashion, distinct from fusion-based approaches (Fang et al., 2013; Ancuti et al., 2018, 2011) using several inputs derived from the raw image and their weight maps.

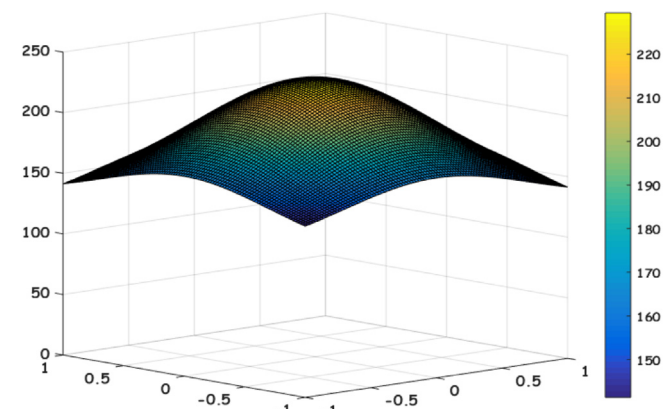


Fig. 2. The intensity distribution of each channel of underwater image using the color correction method (Fu et al., 2014). Note that the intensity value of color-corrected underwater image can be redistributed in a reasonable range, which can avoid underwater image under-enhancement and over-enhancement.

3. Bayesian retinex underwater image enhancement

The Bayesian retinex approach for enhancing single underwater image will be elaborated in this section. The overview of the proposed method is first described, and then three modules of color correction, Bayesian retinex image enhancement, and illumination adjustment will be detailed subsequently.

3.1. Overview

The overview of the proposed approach is presented as follows. First, a simple yet effective color correction method is used to deal with a degraded underwater image S for restoring its color and naturalness. When acquiring the color-corrected underwater image U , and following the pioneering works (Fu et al., 2014; Yue et al., 2017) of both avoiding potential color artifacts generated from illumination adjustment and reducing computing complexity, U is converted from RGB space into HSV space (Sattar and Dudek, 2006; Sattar et al., 2005) which is more robust to illumination variations, and the proposed model is performed on the value channel L in HSV space, which is different from previous image enhancement methods generally implemented on RGB channels. The retinex theory (Land, 1964; Land and McCann, 1971) shows that human visual system can deal with illumination that adaptively varies brightness and color, and retinex-based methods can be used to solve the problems of under-exposure and blurring due to the variation of underwater environment similar to that of the illumination. Then L is decomposed into the illumination component I and the reflectance component R , and the proposed Bayesian retinex model is performed to enhance I and R simultaneously. After that, a Gamma correction (Fu et al., 2015; Li et al., 2016b; Ng and Wang, 2011; Kimmel et al., 2003) method is adopted to adjust the enhanced illumination, and the enhanced value channel image L_e is yielded by a product of the adjusted illumination I_e and the enhanced reflectance. In the end, the final enhanced image is generated by transforming the enhanced HSV image to RGB space. The three modules of color correction, Bayesian retinex image enhancement, and illumination adjustment will be detailed in following subsections.

3.2. Color correction

Due to special underwater imaging and lighting conditions, underwater images easily suffer from serious color casts, and most degraded underwater images appear greenish or bluish. As shown in Fig. 1(b), different wavelengths of light are attenuated at different rates in the water, specifically, the red light first disappears at depth of 5 m due

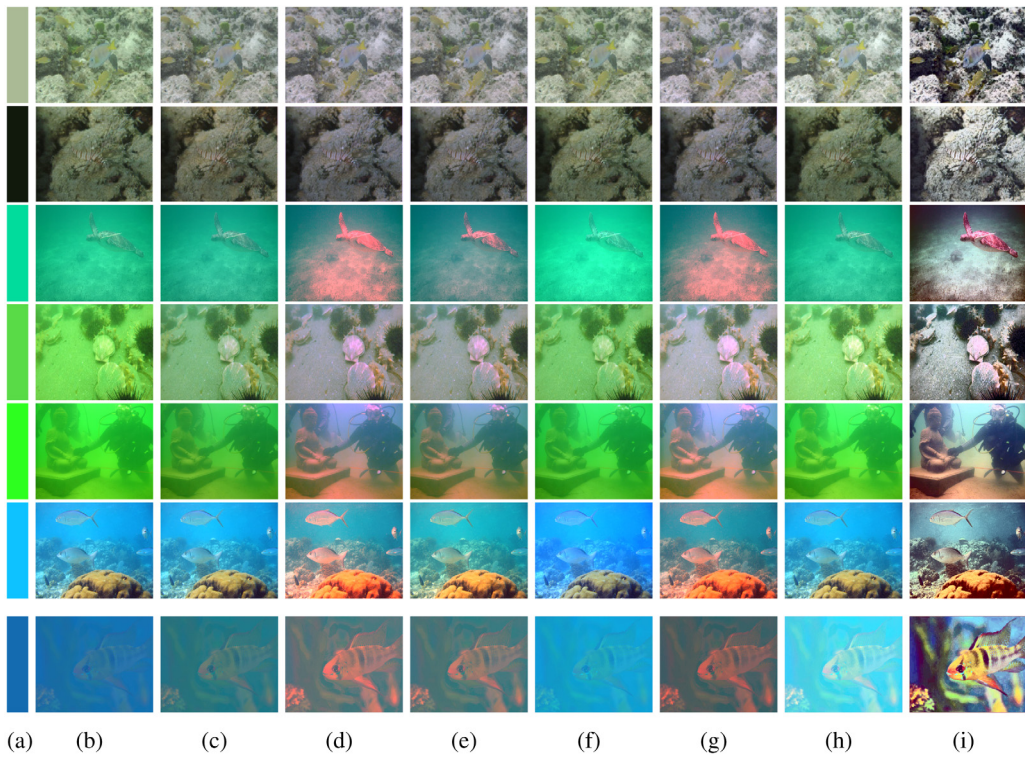


Fig. 3. Color correction comparison. (a) Background light color, (b) Raw image, (c) MaxRGB, (d) Gray-World, (e) Shade-of-Gray, (f) Gray-Edge, (g) White-Balance, (h) White-Patch, (i) Proposed. Note that under different conditions of underwater background color, the proposed method (Proposed) consistently outperforms other color constancy approaches in terms of both color restoration and naturalness preservation. MaxRGB, Gray-Edge and White-Patch cannot remove undesirable color casts, Gray-World and White-Balance generate overcompensation results of red channels, and Shade-of-Gray fails in restoring color in extreme underwater scenes.

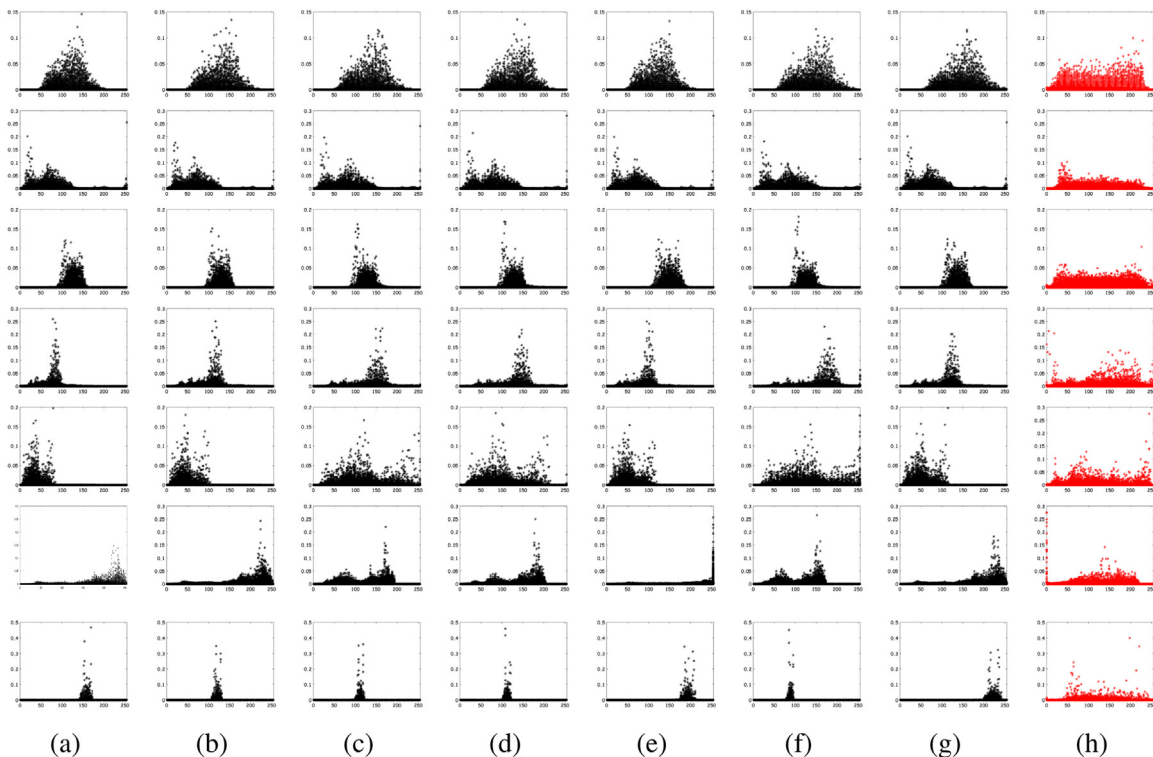


Fig. 4. Color histogram distributions of Fig. 3. (a) Raw image, (b) MaxRGB, (c) Gray-World, (d) Shade-of-Gray, (e) Gray-Edge, (f) White-Balance, (g) White-Patch, (h) Proposed. Note that the color histograms of the proposed method (Proposed) are more evenly distributed in the whole range, while the histogram distributions of other methods are more concentrated around particular values or ranges.

to its longest wavelength or minimum energy, and then brown and yellow lights disappear at depths of 10 m and 20 m respectively, while the green and blue lights finally disappear at depths of 30 m and 60 m respectively due to their shorter wavelength or larger energy. This is the main reason that most degraded underwater images are dominated by blue or green coloration, and color casts lead to the poor visual quality of underwater images. Therefore, it is first desirable to remove color casts and restore relatively genuine color of underwater images, and a simple but effective color correction based on statistical method (Fu et al., 2014) is adopted to address color casts, and the color corrected image \mathbf{U} can be calculated by

$$\mathbf{U}_c = \frac{255}{2} \times \left(1 + \frac{\mathbf{S}_c - \mathbf{M}_c}{\mu \mathbf{V}_c}\right) \quad (1)$$

where $c \in \{R, G, B\}$, and the operation (1) is respectively performed on each channel [red (R), green(G) and blue (B)] of the degraded underwater image \mathbf{S} . \mathbf{M}_c and \mathbf{V}_c are the mean value and the variance in the c channel \mathbf{S}_c , respectively. μ is a parameter to temper the saturation of underwater enhanced result, and it is empirically set to 2.5 for each color channel. In Fig. 2, the intensity distribution of each color channel of the underwater image is displayed by using the color correction method (Fu et al., 2014), and it is noted that the intensity value of the color-corrected underwater image is redistributed in a certain range [140, 240], which can reasonably avoid underwater image under-enhancement and over-enhancement. Furthermore, Fig. 3 shows the underwater color correction results of the proposed method (Proposed) and different color constancy approaches including MaxRGB (Land, 1977), Gray-World (Buchsbaum, 1980), Shade-of-Gray (Finlayson and Trezzi, 2004), Gray-Edge (van de Weijer et al., 2007), White-Balance (Ebner, 2007), White-Patch (Ebner, 2007), and one can see that the proposed method consistently yields better visual results of color correction and naturalness preservation than other color constancy methods under different conditions of underwater background color. As seen in Fig. 3(c), (f) and (h), MaxRGB, Gray-Edge and White-Patch cannot remove undesirable color casts, and their restoration results appear bluish and greenish. Gray-World and White-Balance have slight results of color correction in shallow underwater background, but some overcompensation results of red channels shown in Fig. 3(d) and (g) are generated in the deep underwater background. In Fig. 3(e), Shade-of-Gray cannot remove color casts in extremely deteriorated underwater scenes. Moreover, Fig. 4 illustrates corresponding color histogram distributions of the enhanced images using the proposed method and other competitive method in Fig. 3. It is noted that the color histograms of the proposed method (Proposed) (Fig. 4(h)) are more evenly redistributed in the whole range, while the histogram distributions of other competitive methods are more concentrated around particular values or ranges shown in Fig. 4(a)–(g). The above results reveal that the proposed method yields more reasonable and effective color histogram distributions than other methods. Most of the above color constancy methods make a specific assumption that estimates the color of the light source and then achieves color constancy by dividing each color channel by its corresponding normalized light source intensity. However, there are two unreasonable aspects for this assumption: one is that degraded underwater images are usually generated with highly attenuated red channels, and a very small mean value for the red channels is produced to lead to an overcompensation in the locations where red is present since this assumption divides each channel by its mean value. The representative results are seen in the enhanced images of Gray-World, White-Balance and Shade-of-Gray. The other is that white patches are not common in degraded underwater images, and even a white patch is in the scene, this patch reflects maximum light possible for each band and will be the illuminant color. The corresponding methods such as MaxRGB and White-Patch can remove the part color of the light source, but their color results cannot be restored well. In addition, a deeper observation is made that under extremely deteriorated underwater scenes, above color constancy approaches perform poorly in removing color casts, and their corrected images present generally bluish or greenish.

3.3. Bayesian retinex image enhancement

(1) Model Construction Following the previous works (Fu et al., 2014; Yue et al., 2017) that reduce computing complexity and avoid potential color artifacts, the color-corrected underwater image \mathbf{U} is transformed from RGB color space into HSV color space, and then the proposed model is performed on the value channel image \mathbf{L} in HSV space. The retinex theory (Land, 1964; Land and McCann, 1971) demonstrates that the human visual system can be adaptive to handle the illumination that varies brightness and color, and retinex-based methods can be used to solve the problems of under-exposure and blurring. The classic retinex model can be expressed as $\mathbf{O} = \mathbf{I} \cdot \mathbf{R}$, where \mathbf{I} and \mathbf{R} denote the illumination (within the range [0, 255]) and the reflectance (within the range [0, 1]) of an image \mathbf{O} (within the range [0, 255]), respectively. The \cdot operator denotes the element-wise multiplication. On the basis of above retinex enhancement mechanism, \mathbf{L} is decomposed into the illumination component \mathbf{I} and the reflectance component \mathbf{R} , and the proposed Bayesian retinex enhancement model is performed to enhance \mathbf{I} and \mathbf{R} simultaneously. By the Bayes theorem, the proposed retinex probabilistic model for enhancing \mathbf{I} and \mathbf{R} is formulated as a posterior distribution:

$$p(\mathbf{I}, \mathbf{R}|\mathbf{L}) \propto p(\mathbf{L}|\mathbf{I}, \mathbf{R})p(\mathbf{I})p(\mathbf{R}) \quad (2)$$

where $p(\mathbf{I}, \mathbf{R}|\mathbf{L})$ is the posterior distribution, $p(\mathbf{L}|\mathbf{I}, \mathbf{R})$ represents the likelihood, $p(\mathbf{I})$ and $p(\mathbf{R})$ denote the priors on the illumination and the reflectance respectively. In the following, these terms are defined as follows:

Likelihood $p(\mathbf{L}|\mathbf{I}, \mathbf{R})$. The likelihood of the value channel image \mathbf{L} is based on the retinex decomposition that \mathbf{L} can be ideally seen as a product of the illumination \mathbf{I} and the reflectance \mathbf{R} . The estimated error $\mathbf{e} = \mathbf{L} - \mathbf{I} \cdot \mathbf{R}$ is modeled as a set of independent and identically distributed (i.i.d.) noise random variables with a Gaussian distribution with zero mean and variance σ^2 . The likelihood $p(\mathbf{L}|\mathbf{I}, \mathbf{R})$ is defined as

$$p(\mathbf{L}|\mathbf{I}, \mathbf{R}) = \mathcal{N}(\mathbf{e}|0, \sigma^2 \mathbf{1}) \quad (3)$$

where \cdot denotes the element-wise multiplication operator, and $\mathbf{1}$ represents the identity matrix.

Prior $p(\mathbf{R})$. For capturing more fine-scale and complete structures from underwater images, multiorder gradient priors are introduced to design $p(\mathbf{R})$. There are abundant image structures, including large-scale edges and more fine-scale details, in first-order and second-order gradients of the reflectance in Fig. 5(e), (f) and (g). And it is clearly observed that the histogram distributions of the multiorder gradients of the reflectance shown in Fig. 5(k), (l), (m) are more sparse than those of the illumination in Fig. 5(n), (o), (p). Based on above properties of the reflectance, two priors are adopted to model piecewise and piecewise linear components of the reflectance. One is the total variation prior (Fu et al., 2014; Yue et al., 2017; Fu et al., 2015), which assumes that the reflectance is piecewise continuous, and the first-order gradient distribution of the reflectance is seen as a Laplacian distribution with location zero and scale s_1 :

$$p_1(\mathbf{R}) = \mathcal{L}(\nabla \mathbf{R}|0, s_1 \mathbf{1}) \quad (4)$$

where ∇ is the gradient operator in both the horizontal and vertical directions. Another is the second-order gradient prior imposed on the reflectance to capture higher-order edges of relatively smaller scale in the gradient domain and suppress potential staircase artifacts. The second-order derivative distribution of the reflectance can be formulated as a Laplacian distribution with location zero and scale s_2 :

$$p_2(\mathbf{R}) = \mathcal{L}(\Delta \mathbf{R}|0, s_2 \mathbf{1}) \quad (5)$$

where $\Delta = [0, 1, 0; 1, -4, 1; 0, 1, 0]$ is a second-order Laplacian filter. Therefore, the final prior $p(\mathbf{R})$ is written as

$$p(\mathbf{R}) = p_1(\mathbf{R})p_2(\mathbf{R}) \quad (6)$$

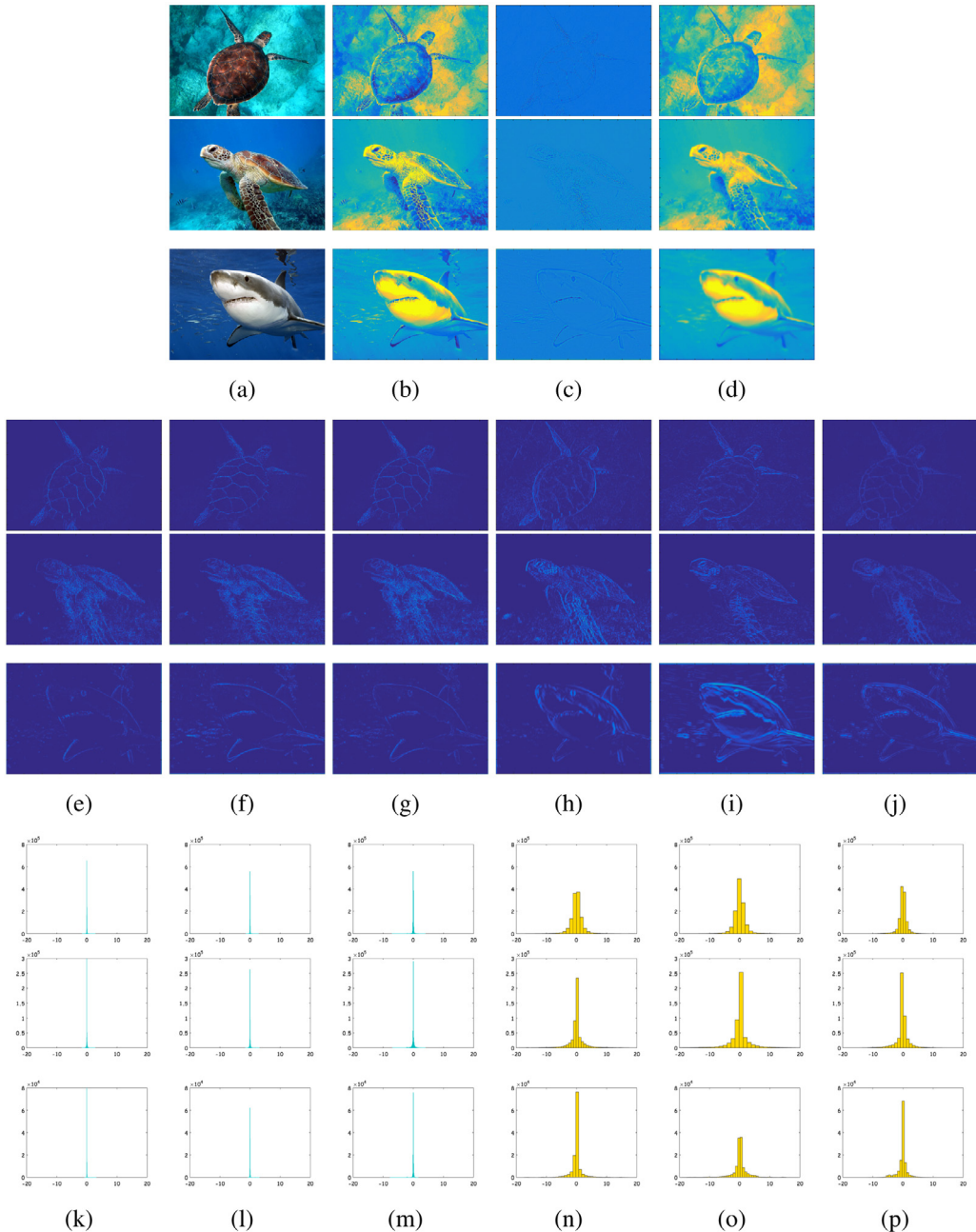


Fig. 5. Multiorder gradient priors of reflectance and illumination in HSV-color space. (a) high-quality underwater image. (b) the value channel. (c) the reflectance. (d) the illumination. (e)–(f) and (h)–(i) are the first-order gradient in horizontal and vertical directions of (c) and (d), respectively. (g) and (j) are the second-order gradient of (c) and (d), respectively. (k)–(p) are the histogram distributions of (e)–(j), respectively. Note that there are abundant image structures in first-order and second-order gradients of both reflectance and illumination. The reflectance contains large-scale edges and more fine-scale details, and its multiorder gradients have more sparse histogram distributions than those of the illumination. Meanwhile, the illumination has complementary image structures and presents relative smoother than the reflectance.

Prior $p(\mathbf{I})$. First-order and second-order gradient priors are imposed to design $p(\mathbf{I})$, which acquires complementary and complete structures (Fig. 5(h)–(j) and (d)) from underwater images by enforcing spatial smoothness and linear smoothness of the illumination. And as shown in Fig. 5(c)–(d) and (e)–(j), the illumination is revealed to be relative smoother than the reflectance. One models a piecewise prior on the first-order gradient distribution of the illumination. To enforce the spatial smoothness of the illumination, a Gaussian distribution with zero mean and variance σ_3^2 is adopted to model the first-order gradient prior of the illumination:

$$p_1(\mathbf{I}) = \mathcal{N}(\nabla \mathbf{I} | 0, \sigma_3^2 \mathbf{1}) \quad (7)$$

Another is second-order gradient prior that models an approximation on piecewise linear components of the illumination since its nature follows certain paths. And another Gaussian distribution with zero mean and variance σ_4^2 is employed to model the second-order derivative prior of the illumination:

$$p_2(\mathbf{I}) = \mathcal{N}(\Delta \mathbf{I} | 0, \sigma_4^2 \mathbf{1}) \quad (8)$$

Finally, the prior $p(\mathbf{I})$ is calculated by

$$p(\mathbf{I}) = p_1(\mathbf{I})p_2(\mathbf{I}) \quad (9)$$

Objective $E(\mathbf{I}, \mathbf{R})$. In order to estimate the reflectance and the illumination simultaneously, the maximum a posteriori (MAP) problem

is transformed to an energy minimization problem, namely, $E(\mathbf{I}, \mathbf{R}) = -\log(p(\mathbf{I}, \mathbf{R}|\mathbf{L}))$. Then the objective function is established by taking all likelihood and prior definitions into (2):

$$\begin{aligned} E(\mathbf{I}, \mathbf{R}) = & \|\mathbf{I} \cdot \mathbf{R} - \mathbf{L}\|_2^2 + v_1 \|\nabla \mathbf{R}\|_1 + v_2 \|\Delta \mathbf{R}\|_1 \\ & + v_3 \|\nabla \mathbf{I}\|_2^2 + v_4 \|\Delta \mathbf{I}\|_2^2 \quad \text{s.t. } \mathbf{L} \leq \mathbf{I} \end{aligned} \quad (10)$$

where $\|\cdot\|_p$ denotes the p -norm operator, and the parameters $\{v_i\}_{i=1}^4$ ($v_i = \sigma^2/s_i$ when $i = 1, 2$, and $v_i = \sigma^2/\sigma_i^2$ when $i = 3, 4$) are positive to balance above terms. The anisotropic total variation (TV) is used to enforce better sparsity on image structures than the isotropic TV (Chan et al., 2005; Grasmair and Lenzen, 2010). It is noted that the l_1 norm is appropriately adopted to model piecewise constant and piecewise linear approximations on the reflectance since it is observed to be more sparse than the illumination, and the l_2 norm is effectively employed to enforce spatial smoothness and linear smoothness on the illumination since it is shown to be relative smoother than the reflectance. The role of each term in (10) is interpreted respectively:

- $\|\mathbf{I} \cdot \mathbf{R} - \mathbf{L}\|_2^2$ denotes the data fidelity, which imposes the l_2 norm to minimize the error between the value channel image \mathbf{L} and the estimation $\mathbf{I} \cdot \mathbf{R}$.
- $\|\nabla \mathbf{R}\|_1$ is the first-order TV prior that uses the appropriate l_1 norm to enforce the piecewise continuous on the reflectance \mathbf{R} .
- $\|\Delta \mathbf{R}\|_1$ is the second-order TV prior that employs the l_1 norm suitably to ensure the sparsity of piecewise linear components of the reflectance.
- $\|\nabla \mathbf{I}\|_2^2$ ensures the piecewise continuous on the illumination \mathbf{I} , and the l_2 norm is effectively used to enforce the gradient sparsity of the illumination.
- $\|\Delta \mathbf{I}\|_2^2$ adopts the effective l_2 norm to enforce the sparsity of piecewise linear components of the illumination.
- $\mathbf{L} \leq \mathbf{I}$ guarantees the prior that \mathbf{R} is ranged from 0 to 1.

(2) Numerical Solution Traditional gradient descent methods are unsuitable for addressing (10) where there are two unknown variables \mathbf{I} and \mathbf{R} , fortunately, an efficient iterative optimization scheme is developed to seek for an optimal solution to (10) by using an alternating direction method of multipliers (ADMM) (Boyd et al., 2011; Goldstein and Osher, 2009) with fast operations of shrinkage thresholding and fast Fourier transform (FFT) (Ng and Wang, 2011; Xu and Jia, 2010). Directly optimizing (10) is intractable since the two l_1 norms are difficult to be solved, two auxiliary variables \mathbf{d}, \mathbf{h} , and two errors \mathbf{m}, \mathbf{n} are introduced to reformulate (10) into the following form:

$$\begin{aligned} E(\mathbf{I}, \mathbf{R}) = & \|\mathbf{I} \cdot \mathbf{R} - \mathbf{L}\|_2^2 + v_1 \{\|\mathbf{d}\|_1 + \lambda_1 \|\nabla \mathbf{R} - \mathbf{d} + \mathbf{m}\|_2^2\} \\ & + v_2 \{\|\mathbf{h}\|_1 + \lambda_2 \|\Delta \mathbf{R} - \mathbf{h} + \mathbf{n}\|_2^2\} + v_3 \|\nabla \mathbf{I}\|_2^2 \\ & + v_4 \|\Delta \mathbf{I}\|_2^2 \quad \text{s.t. } \mathbf{L} \leq \mathbf{I} \end{aligned} \quad (11)$$

where $\{\lambda_i\}_{i=1}^2$ are the positive scalars to balance above terms. To efficiently address the above complex problem, (11) is transformed into three simple denoising subproblems which can be separately and iteratively cycled through. Their forms at the k th iteration can be expressed as follows:

$$\begin{aligned} (P1) \quad \mathbf{d}^k = & \arg \min_{\mathbf{d}} \|\mathbf{d}\|_1 + \lambda_1 \|\nabla \mathbf{R}^{k-1} - \mathbf{d} + \mathbf{m}^{k-1}\|_2^2 \\ \mathbf{h}^k = & \arg \min_{\mathbf{h}} \|\mathbf{h}\|_1 + \lambda_2 \|\Delta \mathbf{R}^{k-1} - \mathbf{h} + \mathbf{n}^{k-1}\|_2^2 \end{aligned} \quad (12)$$

$$\begin{aligned} (P2) \quad \mathbf{R}^k = & \arg \min_{\mathbf{R}} \|\mathbf{R} - \frac{\mathbf{L}}{\mathbf{I}^{k-1}}\|_2^2 + v_1 \lambda_1 \|\nabla \mathbf{R} - \mathbf{d}^k + \mathbf{m}^{k-1}\|_2^2 \\ & + v_2 \lambda_2 \|\Delta \mathbf{R} - \mathbf{h}^k + \mathbf{n}^{k-1}\|_2^2 \\ \mathbf{m}^k = & \mathbf{m}^{k-1} + \nabla \mathbf{R}^k - \mathbf{d}^k \end{aligned} \quad (13)$$

$$\mathbf{n}^k = \mathbf{n}^{k-1} + \Delta \mathbf{R}^k - \mathbf{h}^k$$

$$(P3) \quad \mathbf{I}^k = \arg \min_{\mathbf{I}} \|\mathbf{I} - \frac{\mathbf{L}}{\mathbf{R}^k}\|_2^2 + v_3 \|\nabla \mathbf{I}\|_2^2 + v_4 \|\Delta \mathbf{I}\|_2^2 \quad (14)$$

It is noted that $\|\mathbf{R} \cdot \mathbf{I}^{k-1} - \mathbf{L}\|_2^2$ and $\|\mathbf{I} \cdot \mathbf{R}^k - \mathbf{L}\|_2^2$ are respectively transformed to $\|\mathbf{R} - \frac{\mathbf{L}}{\mathbf{I}^{k-1}}\|_2^2$ and $\|\mathbf{I} - \frac{\mathbf{L}}{\mathbf{R}^k}\|_2^2$ in (P2) and (P3) for calculation convenience. The three subproblems have closed-form global optimal solutions, and their updating algorithms are detailed below:

Update for P1: Total Variation Approximation. Initialize $\mathbf{R}^0 = 0$, $\mathbf{m}^0 = 0$, $\mathbf{n}^0 = 0$ and $\mathbf{e}^0 = 0$. Then a shrinkage operation is used to update the auxiliary variables \mathbf{d}^k and \mathbf{h}^k at the k th iteration:

$$\begin{aligned} \mathbf{d}_h^k &= \text{shrink}(\nabla_h \mathbf{R}^{k-1} + \mathbf{m}_h^{k-1}, \frac{1}{2\lambda_1}) \\ \mathbf{d}_v^k &= \text{shrink}(\nabla_v \mathbf{R}^{k-1} + \mathbf{m}_v^{k-1}, \frac{1}{2\lambda_1}) \\ \mathbf{h}^k &= \text{shrink}(\Delta \mathbf{R}^{k-1} + \mathbf{n}^{k-1}, \frac{1}{2\lambda_2}) \end{aligned} \quad (15)$$

where $\text{shrink}(x, \lambda) = \frac{x}{|x|} * \max(|x| - \lambda, 0)$, and $\frac{x}{|x|} = 0$ if $|x| = 0$. $\nabla_h = [-1, 1]$ and $\nabla_v = [-1; 1]$ denote the first-order derivative operator at horizontal and vertical directions, respectively.

Update for P2: Reflectance Reconstruction. Similar to center/surround retinex enhancement methods (Rahman et al., 2004; Jobson et al., 1997), \mathbf{I}^0 is initialized to be a Gaussian lowpass filtering of \mathbf{L} . \mathbf{R}^k has a closed-form solution since P2 is a least square problem which involves three convex functions. Then the first-order derivative of (13) is set to 0, and the fast Fourier transformation (FFT) (Ng and Wang, 2011; Xu and Jia, 2010) is adopted to speed up the solving process. Thus the closed-form solution \mathbf{R}^k is updated by the following expression:

$$\mathbf{R}^k = \mathcal{F}^{-1} \left\{ \frac{\mathcal{F}(\mathbf{L}/\mathbf{I}^{k-1}) + v_1 \lambda_1 \boldsymbol{\Phi}_1 + v_2 \lambda_2 \boldsymbol{\Phi}_2}{\mathcal{F}(\mathbf{I}) + v_1 \lambda_1 \boldsymbol{\Psi}_1 + v_2 \lambda_2 \boldsymbol{\Psi}_2} \right\} \quad (16)$$

where $\boldsymbol{\Phi}_1 = \mathcal{F}^*(\nabla_h) \cdot \mathcal{F}(\mathbf{d}_h^k - \mathbf{m}_h^{k-1}) + \mathcal{F}^*(\nabla_v) \cdot \mathcal{F}(\mathbf{d}_v^k - \mathbf{m}_v^{k-1})$, $\boldsymbol{\Phi}_2 = \mathcal{F}^*(\Delta) \cdot \mathcal{F}(\mathbf{h}^k - \mathbf{n}^{k-1})$, $\boldsymbol{\Psi}_1 = \mathcal{F}^*(\nabla_h) \cdot \mathcal{F}(\nabla_h) + \mathcal{F}^*(\nabla_v) \cdot \mathcal{F}(\nabla_v)$, and $\boldsymbol{\Psi}_2 = \mathcal{F}^*(\Delta) \cdot \mathcal{F}(\Delta)$. \mathcal{F} denotes the FFT operator, \mathcal{F}^* and \mathcal{F}^{-1} are conjugate transpose and inverse operators of \mathcal{F} , respectively. The first-order and second-order derivative operators are diagonalized using the FFT for avoiding matrix inversion, and all calculations are performed component-wise. Then \mathbf{m}^k and \mathbf{n}^k are updated by following from ADMM:

$$\begin{aligned} \mathbf{m}_h^k &= \mathbf{m}_h^{k-1} + \nabla_h \mathbf{R}^k - \mathbf{d}_h^k \\ \mathbf{m}_v^k &= \mathbf{m}_v^{k-1} + \nabla_v \mathbf{R}^k - \mathbf{d}_v^k \\ \mathbf{n}^k &= \mathbf{n}^{k-1} + \Delta \mathbf{R}^k - \mathbf{h}^k \end{aligned} \quad (17)$$

The above operations are akin to adding back the noise in TV denoising (Osher et al., 2005).

Update for P3: Illumination Reconstruction. Similar to (13), the illumination \mathbf{I}^k has a closed-form solution since P3 is a least square problem. The first-order derivative is taken on (14), and it is set to 0. Then FFT is used to speed up the process, and the closed-form solution \mathbf{I}^k is updated by

$$\mathbf{I}^k = \mathcal{F}^{-1} \left\{ \frac{\mathcal{F}(\mathbf{L}/\mathbf{R}^k)}{\mathcal{F}(\mathbf{I}) + v_3 \boldsymbol{\Psi}_1 + v_4 \boldsymbol{\Psi}_2} \right\} \quad (18)$$

All the above calculations are performed component-wise. Following the pioneering work (Fu et al., 2015), the updated illumination is corrected through $\mathbf{I}^k = \max(\mathbf{I}^k, \mathbf{L})$, which aims to meet the constraint $\mathbf{L} \leq \mathbf{I}$ in (11).

Since fast operations of FFT and shrinkage operation are performed at few iterations, \mathbf{I} and \mathbf{R} can be estimated simultaneously and efficiently. In the end, the main steps of proposed algorithm are summarized in Algorithm 1. Furthermore, the existence of a solution to the problem (10) and the convergence analysis of corresponding transformed subproblems are mathematically provided in Appendix.

3.4. Illumination adjustment

After estimating the reflectance and the illumination, the illumination is adjusted to enhance underwater image details in the following task. Since the reflectance derived from retinex is sometimes overen-

Algorithm 1 Outline of Proposed Algorithm

Input: input value channel \mathbf{L} , weighting parameters $\{v_i\}_{i=1}^4$ and $\{\lambda_i\}_{i=1}^2$, and maximum iteration number T .
Initialization: $\mathbf{I}^0 \leftarrow$ Gaussian filtering of \mathbf{L} , $\mathbf{R}^0 = 0$, $\mathbf{m}^0 = 0$, $\mathbf{n}^0 = 0$, and $k = 1$.
Iteration on $k = 1, \dots, T$:
update \mathbf{d}^k and \mathbf{h}^k via Eq. (15).
update \mathbf{R}^k via Eq. (16).
update \mathbf{m}^k and \mathbf{n}^k via Eq. (17).
update \mathbf{I}^k via Eq. (18).
Stopping criteria: terminate iteration if $k = T$, otherwise, continue iteration and $k \leftarrow k + 1$.
Output: enhanced reflectance \mathbf{R} and illumination \mathbf{I} .

hanced, an effective Gamma correction operation (Yue et al., 2017; Fu et al., 2015; Ng and Wang, 2011; Kimmel et al., 2003) is adopted after the decomposition, and the illumination \mathbf{I} with an adjustment parameter γ is corrected as

$$\mathbf{I}_e = \mathbf{W} \left(\frac{\mathbf{I}}{\mathbf{W}} \right)^{\frac{1}{\gamma}} \quad (19)$$

According to the default settings in Yue et al. (2017), Fu et al. (2015), the empirical parameters \mathbf{W} and γ are set as 255 and 2.2, respectively. And the final value channel image \mathbf{L}_e is calculated below:

$$\mathbf{L}_e = \mathbf{I}_e \cdot \mathbf{R} \quad (20)$$

Consequently, the final enhanced underwater image is generated by transforming the enhanced HSV underwater image to RGB space.

4. Experimental results

In this section, numerous experiments are provided to demonstrate the effectiveness of the proposed algorithm in underwater image enhancement. First, experimental settings, all comparing algorithms and evaluation metrics are presented. Then underwater image enhancement results of the proposed approach and several traditional and state-of-the-art underwater image enhancement methods are compared in both qualitative and quantitative assessments. Meanwhile, color accuracy test, structural enhancement comparison, and challenging underwater scenes comparison are carried out respectively. After that, an ablation study is performed to investigate the effect of each component of the proposed method, and the proposed method is compared with the edge-preserving filtering retinex method. Another extensive study is conducted to evaluate the impact of model parameters. Convergence analysis and computational complexity of the proposed method are discussed subsequently. Finally, extended experiments are provided on several applications in terms of underwater keypoint detection, underwater saliency detection, underwater depth map estimation, and underwater image segmentation.

4.1. Experiment setting

To evaluate the comprehensive performance of the proposed method, many underwater images from various scenes are tested. 50 raw underwater images are randomly collected from Ancuti et al. (2012), Galdran et al. (2015), Chiang and Chen (2012), Fu et al. (2014, 2017), Li et al. (2016a, 2017), and these images tested in Fig. 6 can be available at the website: <https://github.com/zhuangpeixian/50UData>. All experiments are performed on a PC with Intel Core i7-4790 CPU (3.60 GHz), 8G RAM and 64-bit Windows7 operating system, using Matlab R2019a software. In the following experiments, the regularization parameters v_1 , v_2 , v_3 , and v_4 are empirically set as 1, $1e - 3$, $1e - 5$, and $1e - 3$, respectively. The shrinkage thresholding parameters λ_1 and λ_2 are appropriately set to $1e - 4$ and $1e - 3$, respectively. For the stopping

parameter, the number of maximum iteration T is set to be 8, which is sufficient to generate decent enhanced results by taking account of a better trade off between algorithm convergence and computational efficiency. These empirical parameter settings generate decent results for most underwater images, and the analysis of parameter selection is discussed in the experiment of parameter evaluation presented later.

4.2. Algorithms and metrics

To demonstrate the effectiveness of our method, the proposed method is compared with the following twenty-two underwater image enhancement approaches:

- MaxRGB: Maximum response in each channel of RGB caused by a white patch (Land, 1977).¹
- Gray-World: Gray World assumption of the achromatic of average reflectance in the scene (Buchsbaum, 1980).¹
- Shade-of-Gray: Minkowski p -norm applied to native pixels (Finlayson and Trezzi, 2004).¹
- Gray-Edge: Minkowski p -norm applied to derivative image structures (van de Weijer et al., 2007).¹
- White-Balance: Colors adjustment matched the inherent color of the object with removing color casts (Ebner, 2007).²
- White-Patch: White Patch assumption of the maximum response in RGB-channels caused by a white patch (Ebner, 2007).³
- SSR: Single Scale Retinex with color restoration (Jobson et al., 1997).³
- MSRCR: Multi-Scale Retinex with Color Restoration (Rahman et al., 2004).³
- CLAHE: Contrast Limited Adaptive Histogram Equalization (Vasamsetti et al., 2017).
- FVR: Fast Visibility Restoration based on median filter (Tarel and Hautiere, 2009).⁴
- WCID: Wavelength Compensation and Image Dehazing (Chiang and Chen, 2012)⁵.
- VRE: Variational Retinex-based Enhancement (Fu et al., 2014).⁶
- ARC: Automatic Red-Channel restoration (Galdran et al., 2015).⁷
- UDCP: Underwater Dark Channel Prior (Drews et al., 2016).⁸
- NLD: Non-Local image Dehazing (Berman et al., 2016).⁹
- MSCW: Multi-Scale Correlated Wavelet (Liu et al., 2017).¹⁰
- DHDP: Dehazing with minimum information loss and Histogram Distribution Prior (Li et al., 2016a).¹¹
- IBIA: Image Blurriness and Light Absorption (Peng and Cosman, 2017).
- TSE: Two-Step Enhancement (Fu et al., 2017).¹²
- WSCT: Weakly Supervised Color Transfer (Li et al., 2018a).
- UGAN: Underwater Generative Adversarial Networks (Fabri et al., 2018).¹³
- MDGAN: Multi-scale Dense Generative Adversarial Network (Guo et al., 2020).

¹ <http://lear.inrialpes.fr/people/vandeweijer/research.html>

² <https://devblogs.nvidia.com/prototyping-algorithms-and-testing-cuda-kernels-matlab/>

³ <https://github.com/whdcumt/ColorConstancy>

⁴ <https://github.com/zhenlab/UnderwaterImageRestoration>

⁵ <https://github.com/mohitkumarahuja/Underwater-Image-Enhancement-by-Wavelength-Compensation-and-Dehazing>

⁶ <http://smartdsp.xmu.edu.cn/underwater.html>

⁷ https://github.com/Mr-Bright/code_review_Automatic-Red-channel-underwater-image-restoration

⁸ <http://www.paulo.c3.furg.br/>

⁹ <http://www.eng.tau.ac.il/~berman/NonLocalDehazing/>

¹⁰ <https://github.com/starxliu/waveletdehaze-sourcecode-v1.0>

¹¹ <https://github.com/Li-Chongyi/TIP2016-code>

¹² <http://smartdsp.xmu.edu.cn/UnderwaterAppendix.html>

¹³ <http://irvlab.cs.umn.edu/enhancing-underwater-imagery-using-generative-adversarial-networks>



Fig. 6. 50 raw underwater images used in following experiments contain different types of background colors, blurring degrees, and underwater objects.

Meanwhile, the performance of the proposed method and above underwater image enhancement methods is quantified by employing the following non-reference evaluation metrics:

- UIQM: Underwater Image Quality Measure (Panetta et al., 2015).¹⁴ The UIQM is a linear composition of three underwater image attribute measures: Underwater Image Sharpness Measure (UISM), Underwater Image Contrast Measure (UIConM), and Underwater Image Colorfulness Measure (UICM). The UIQM measures three important underwater image quality criterions: colorfulness, sharpness, and contrast, and the three weighted parameters are empirically recommended to be 0.2953, 3.5753, and 0.0282, respectively. The higher UIQM values indicate a better balance among colorfulness, sharpness and contrast in the image.
- UCIQE: Underwater Color Image Quality Evaluation (Yang and Sowmya, 2015).¹⁵ The UCIQE is a linear combination of chroma, saturation, and contrast, which can quantify non-uniform color cast, blurring and low-contrast for underwater images. Three weighted parameters are defaulted to be 0.4680, 0.2745, and 0.2576, respectively. The higher UCIQE values denote the image has better tradeoff among chroma, saturation, and contrast.
- CCF: A combination index of Colorfulness, Contrast and Fog density (Wang et al., 2018).¹⁶ The CCF is a feature-weighted metric with combining colorfulness index, contrast index, and fog density index, which can quantify color loss, blurring, and foggy, respectively. The weighted coefficients are set to 0.17593, 0.61759, and 0.33988, respectively. The higher CCF values mean that the image has better equilibrium among colorfulness, contrast, and fog density.
- Entropy: (Li et al., 2016a). The Entropy represents the average information of an image, and the higher Entropy value of an image means more information contained in the image.
- NIQMC: No-reference Image Quality Metric for Contrast distortion (Gu et al., 2017).¹⁷ The NIQMC evaluates image quality by measuring local details and global histogram of an image, which particularly favors the images of higher contrast. The larger NIQMC values denote better qualities of image contrast.

4.3. Qualitative evaluation

The proposed method is compared with the 22 underwater image enhancement approaches on the above 50 raw underwater images, and

partial enhanced results of different methods on 4 representative underwater images with the backgrounds of turquoise, green, shallow blue, and deep blue are shown in Figs. 7–10 respectively. MaxRGB, Gray-World, Shade-of-Gray, Gray-Edge, White-Balance and White-Patch are unable to remove color casts and enhance underwater image contrast. It is attributed to that the color constancy hypotheses for natural images do not hold in relatively complex underwater imaging environments, and the overcompensation of red channels are found in both Gray-World and White-Balance. The SSR and MSRCR methods yield a failure of color correction and structures enhancement due to inaccurate illumination estimations, moreover, the over-enhancement of red color and the over-darkness of enhanced images are observed in Figs. 7–10(h). VRE can recover the color by adopting an effective color correction scheme, and promote image structures by a variational retinex-based framework. Since first-order gradients are only used, blurred details and over-enhanced results are found in Figs. 7–10(m). CLAHE improves underwater image contrasts in Figs. 7–9(j), but performs poor in extremely deteriorated underwater image. Undesirable artifacts are introduced in Figs. 8–9(j), and color deviations cannot be effectively removed in Figs. 7–10(j). In Figs. 7 and 9(k), slight structural enhancement and color restoration are obtained by FVR, while this method fails in color correction and contrast promotion in Figs. 8 and 10(k). In Figs. 7–9(l), structural blurring and over-greenness color appear in WCID, and it is ineffective in enhancing the underwater image of deep blue background. As shown in Figs. 7 and 9(n), the red restoration and contrast improvement is acquired by ARC, but blurring and limited structures are shown in Figs. 8 and 10(n). UDCP aggravates the effect of color casts and is limited in structural improvements. NLD and MSCW alleviate color shifts and promote contrast relatively in Figs. 7–10(p) and (q), but the restored colors present visually incorrect and unauthentic due to ignoring the high absorption of red channel in underwater conditions. DHDP removes color casts and improves contrast in Figs. 7–9(r), unfortunately, reddish color deviation and artifacts are introduced in Fig. 10(r) due to inaccurate color correction. IBLA has less effects on color correction and contrast improvement due to inaccurate underwater formation model and assumption. TSE increases underwater contrast and eliminates color distortions in Figs. 7–9(t), but produces under-enhanced results of color restoration and structure enhancement in Fig. 10(t). WSCT corrects color distortions and improves structures in Figs. 9 and 10(u), but produces less effects of color restoration and structure promotion in Figs. 7 and 8(u). UGAN and MDGAN turn degraded images into better images of color correction and contrast enhancement in Figs. 7–9(v) and (w), unfortunately, reddish color deviations are introduced. As noted in Figs. 7–10(x), the proposed method not only robustly removes color casts but also effectively promotes contrast when enhancing underwater images with different backgrounds, which demonstrates that the proposed method is

¹⁴ <https://github.com/tkrah108/UIQM>

¹⁵ <https://github.com/paulwong16/UCIQE>

¹⁶ <https://github.com/zhenglab/CCF>

¹⁷ <https://sites.google.com/site/guke198701/publications>

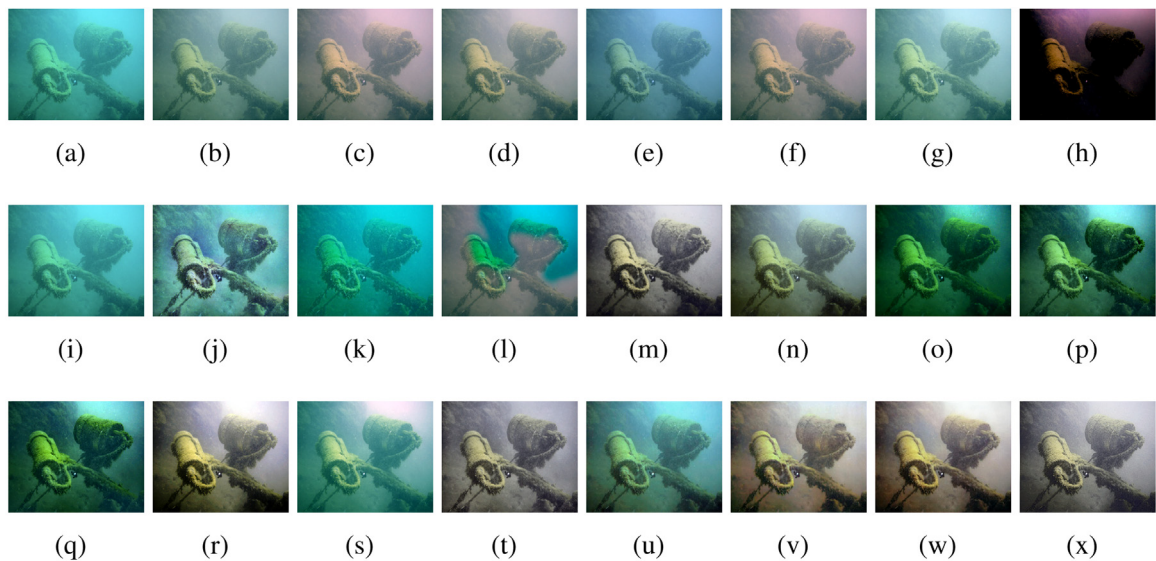


Fig. 7. Comparison of underwater image enhancement results for image Photographic. (a) Raw image, (b) MaxRGB, (c) Gray-World, (d) Shade-of-Gray, (e) Gray-Edge, (f) White-Balance, (g) White-Patch, (h) SSR, (i) MSRCR, (j) CLAHE, (k) FVR, (l) WCID, (m) VRE, (n) ARC, (o) UDCP, (p) NLD, (q) MSCW, (r) DHDP, (s) IBLA, (t) TSE, (u) WSCT, (v) UGAN, (w) MDGAN, (x) OURS. Zoom in all images for better visibility.

more robust to different underwater scenes. It is shown by comparison that the proposed method comprehensively outperforms above non-deep learning and deep learning enhancement approaches in terms of contrast improvement, artifacts or noise suppression, color correction, and naturalness robustness.

4.4. Quantitative assessment

The quantitative results of different methods are evaluated in terms of UIQM, UISM, UIConM, UICM, UCIQE, CCF, Entropy and NIQMC on the above four underwater images and on a tested dataset composed of the 50 raw underwater images, respectively. The comparative results of all indicators for different methods on the four underwater images ‘Photographic’, ‘Turtle’, ‘Tank’, and ‘Fish’ are shown in Fig. 11, and Table 1 reports the average values of eight quantitative evaluations for different methods on the testing set. It is observed that the proposed method obtains higher values of UIQM, UISM, and UIConM than other approaches, meanwhile, the proposed method ranks the fourth best on UICM, comparable to the three leading methods MDGAN, UGAN and DHDP. It is supported that the proposed method achieves better performance together with prominent sharpness improvement, remarkable contrast enhancement, and competitive colorfulness restoration. In Fig. 11(g) and Table 1, the proposed method yields the best Entropy and outperforms other methods in recovering more image information. In CCF measurements, the proposed method is ranked as the second with respect to a promising ability of colorfulness correction, contrast promotion, and fog removal, comparable to DHDP and superior to other rest methods. In UCIQE and NIQMC evaluations, the proposed method is ranked in the third position, and is effective in removing non-uniform color cast and blurring and promoting local details and global contrast. MaxRGB, Gray-World, Shade-of-Gray, Gray-Edge, White-Balance and White-Patch have poor eight measurements due to color constancy hypotheses and overcompensated red channels. The measurements of SSR and MSRCR are lower due to inaccurate illumination estimations, and SSR produces undesirable over-enhanced red and over-darkness results. CLAHE obtains the second best UIConM, but other measurements are unsatisfactory. FVR improves eight indicators to some extent, but its improvement is limited. WCID has improvements in terms of UIQM, UISM, UIConM, UICM, UCIQE and CCF, whereas its Entropy and NIQMC are lower than those of raw underwater images. VRE acquires the second best on Entropy and the third best on CCF, but

its performance is limited by only using first-order gradient priors. ARC, UDCP, NLD and MSCW improve all measurements to a certain degree. MSCW is ranked as the third best on UIQM and UISM, and NLD has higher UCIQE and CCF. DHDP gains the best values of UCIQE, CCF, and NIQMC, the second best UIQM value, the third best values of UIConM and UICM, with respect to an ability to correct color, enhance contrast, and remove haze and blurring, however, reddish color deviation and artifacts appear in Fig. 10(r). IBLA obtains the second best UISM and color corrections reflected in UICM, but its low UIConM demonstrates less positive effect on contrast promotion. TSE achieves the improvement of UIConM, but under-enhanced results appear in Fig. 10(t). WSCT elevates limited improvement of all metrics. The UICM values of MDGAN and UGAN are ranked as the first and second best, and the UCIQE and NIQMC of MDGAN are ranked to be the second-best. In addition, the Entropy of MDGAN is ranked in the third position. However, their reddish deviations emerge in Fig. 10(v) and (w). To sum up, the proposed method yields better quantitative metrics with respect to preferable sharpness and contrast improvement, remarkable blurring and haze removal, and competitive colorfulness restoration. The proposed method are more robust than other methods when testing different underwater scenes.

Besides, an independent user study is performed to provide realistic feedback of users and quantify subjective evaluation of the proposed method. The enhancement results of the 50 raw underwater images are used in this study. For each test image, the enhanced outputs of the 23 algorithms and the raw images are randomly ordered, and all results are displayed on a screen. Then 50 volunteers are separately asked to rank and score each image from 1 to 5 (where 1 denotes the worst quality image and 5 represents the best quality image) subjectively according to quality. The average scores of user study are shown in Fig. 12 from these 1000 trials, and this study demonstrates additional support for the effectiveness of the proposed method in the qualitative evaluation.

4.5. Color accuracy test

To demonstrate the color accuracy of the proposed method, a ColorChecker 24 X-Rite Chart image from Li et al. (2016a) with size of 21 cm×29.7 cm is tested, and it is captured at the depths of 8 m under the Pacific Ocean near the Taiwan. The proposed method is compared with the above 21 methods (add the ground truth and not show poor SSR result) in Fig. 13. When comparing Fig. 13(a) with

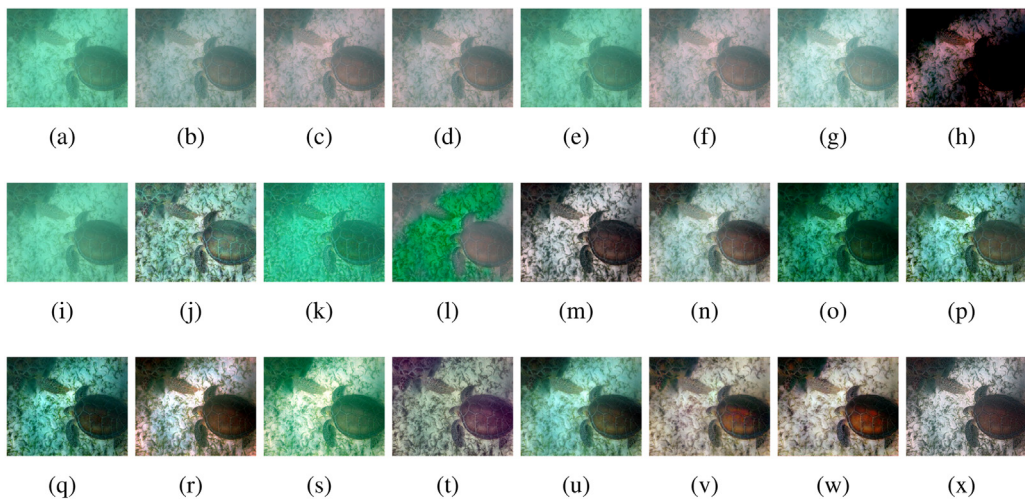


Fig. 8. Comparison of underwater image enhancement results for image Turtle. (a) Raw image, (b) MaxRGB, (c) Gray-World, (d) Shade-of-Gray, (e) Gray-Edge, (f) White-Balance, (g) White-Patch, (h) SSR, (i) MSRCR, (j) CLAHE, (k) FVR, (l) WCID, (m) VRE, (n) ARC, (o) UDCP, (p) NLD, (q) MSCW, (r) DHDP, (s) IBLA, (t) TSE, (u) WSCT, (v) UGAN, (w) MDGAN, (x) OURS. Zoom in all images for better visibility.

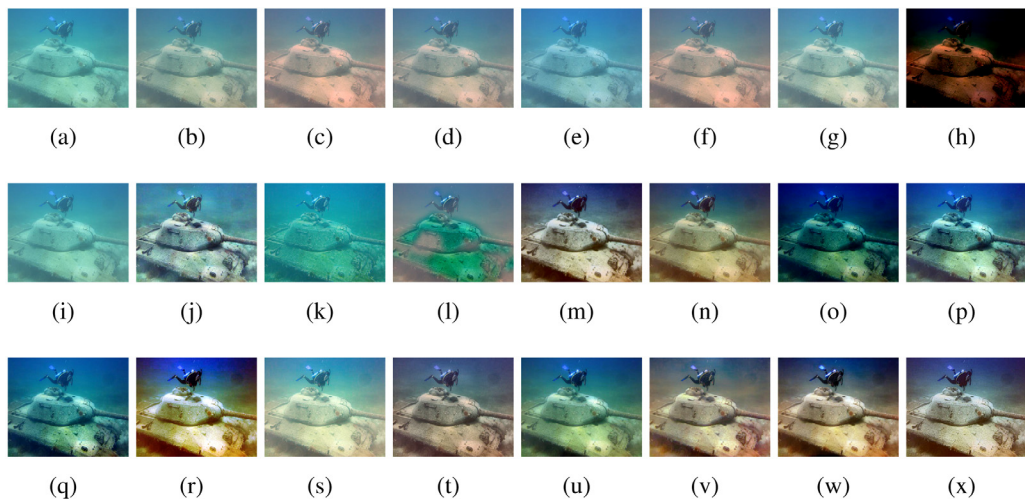


Fig. 9. Comparison of underwater image enhancement results for image Tank. (a) Raw image, (b) MaxRGB, (c) Gray-World, (d) Shade-of-Gray, (e) Gray-Edge, (f) White-Balance, (g) White-Patch, (h) SSR, (i) MSRCR, (j) CLAHE, (k) FVR, (l) WCID, (m) VRE, (n) ARC, (o) UDCP, (p) NLD, (q) MSCW, (r) DHDP, (s) IBLA, (t) TSE, (u) WSCT, (v) UGAN, (w) MDGAN, (x) OURS. Zoom in all images for better visibility.

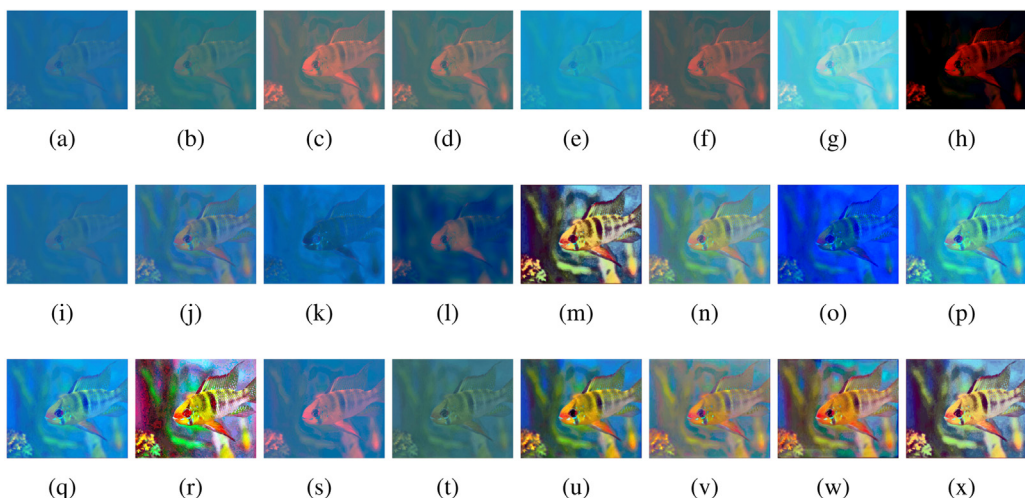


Fig. 10. Comparison of underwater image enhancement results for image Fish. (a) Raw image, (b) MaxRGB, (c) Gray-World, (d) Shade-of-Gray, (e) Gray-Edge, (f) White-Balance, (g) White-Patch, (h) SSR, (i) MSRCR, (j) CLAHE, (k) FVR, (l) WCID, (m) VRE, (n) ARC, (o) UDCP, (p) NLD, (q) MSCW, (r) DHDP, (s) IBLA, (t) TSE, (u) WSCT, (v) UGAN, (w) MDGAN, (x) OURS. Zoom in all images for better visibility.

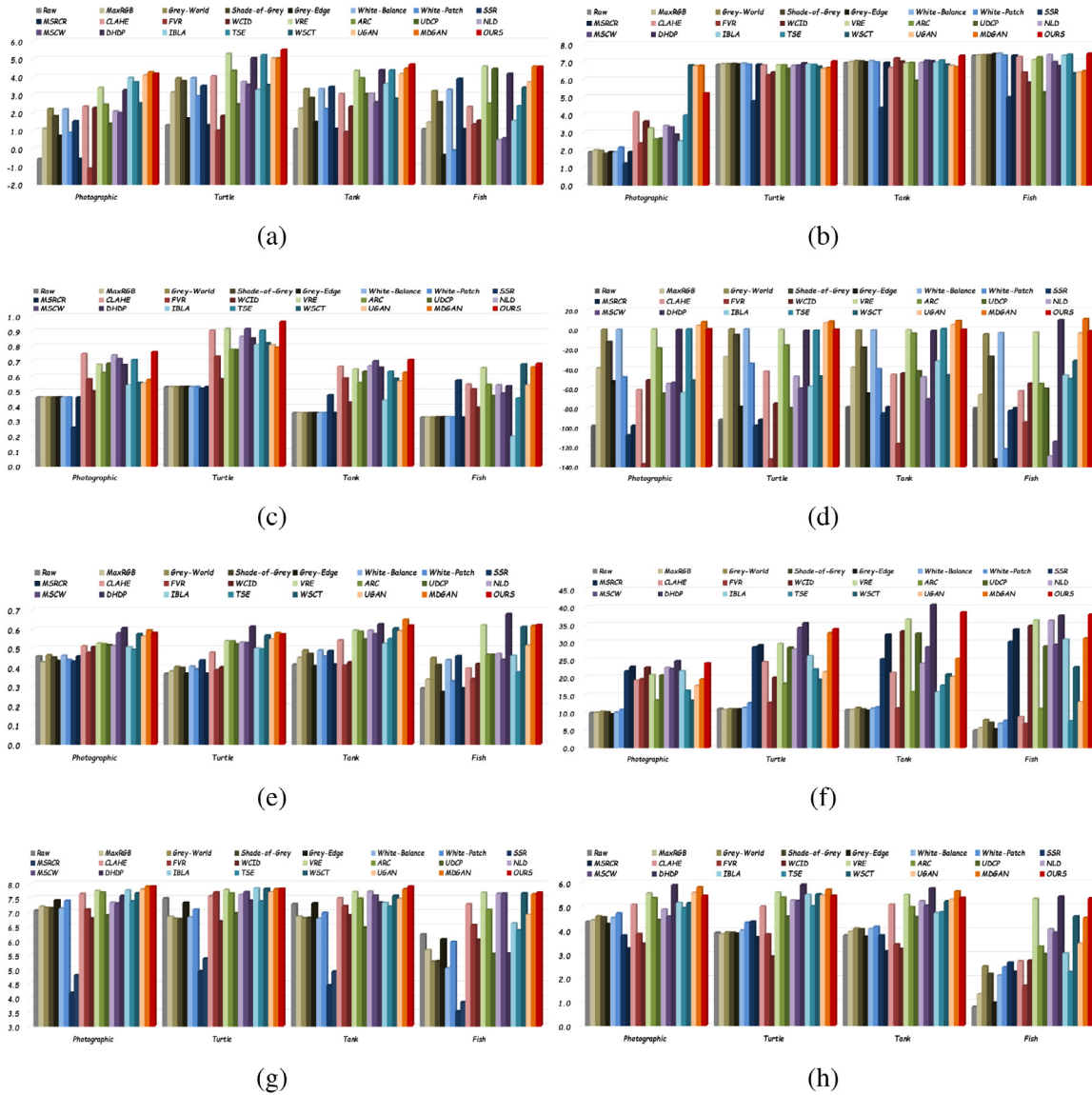


Fig. 11. Comparison of different methods on underwater images ‘Photographic’, ‘Turtle’, ‘Tank’, and ‘Fish’. (a) UIQM, (b) UISM, (c) UIConM, (d) UICM, (e) UCIQE, (f) CCF, (g) Entropy, (h) NIQMC.

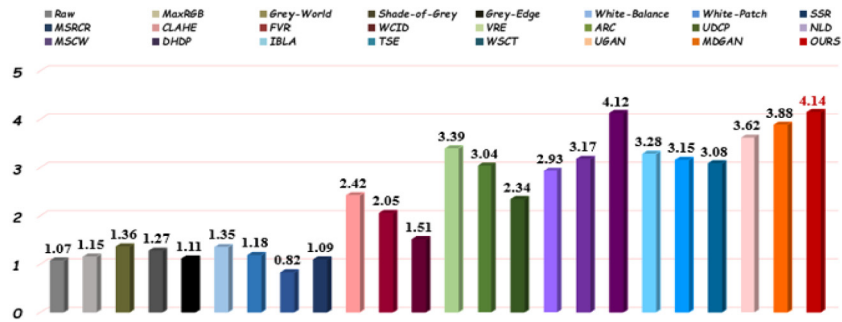


Fig. 12. User study for 50 underwater images.

Fig. 13(b), one can see that some color variations are emerged in the ColorChecker Chart image due to the effects of light scattering and absorption. MaxRGB, Gray-Edge, White-Patch, MSRCR, ARC and WSCT have little effects on correcting the color of the Chart image, while Shade-of-Gray, White-Balance and Gray-World can correct color tone

but not unveil more color details in **Fig. 13(e), (g) and (d)**. **Fig. 13(j)** shows that CLAHE produces a sound effect on removing color cast but introduces observable artifacts, and **Fig. 13(k)** presents undesirable artifacts and color shifts in FVR, such as the colors in the last row and all columns. Although the color is restored soundly in **Fig. 13(l)**,

Table 1

Average quantitative measurements of different methods on 50 underwater images. (Red bold: best, green underline: second best, blue italic: third best).

Methods	UIQM	UISM	UIConM	UICM	UCIQE	CCF	Entropy	NIQMC
Raw	0.4910	5.1735	0.4770	-97.239	0.4270	15.3419	6.7366	3.6922
MaxRGB	1.3561	5.2329	0.4772	-67.211	0.4376	15.4790	6.8740	3.6465
Gray-World	3.0056	5.2362	0.4743	-8.3827	0.5115	18.5482	6.6109	4.0407
Shade-of-Gray	2.3353	5.2499	0.4745	-32.315	0.4753	16.9093	6.6539	3.8825
Gray-Edge	0.8456	5.1169	0.4934	-86.152	0.4347	15.3041	6.9737	3.6126
White-Balance	3.0168	5.2054	0.4705	-7.1783	0.5092	18.1135	6.5721	3.9826
White-Patch	1.1256	5.3918	0.5159	-81.954	0.4528	16.5746	7.0706	3.9729
SSR	0.4830	3.6159	0.4562	-78.575	0.5046	11.5690	3.9390	2.8028
MSRCR	0.4919	5.1860	0.4805	-97.782	0.4370	15.3419	7.1366	3.6922
CLAHE	2.4496	5.7977	<u>0.7123</u>	-64.154	0.5246	16.2955	7.1373	3.9794
FVR	2.9198	6.0572	0.6346	-40.348	0.5358	17.7856	6.9277	3.6962
WCID	2.4503	5.9096	0.5295	-42.126	0.5206	33.0881	6.6199	3.6447
VRE	4.1724	5.8616	0.6976	-1.8649	0.5724	<u>37.1042</u>	<u>7.7042</u>	5.3253
ARC	2.7998	5.3513	0.6269	-36.240	0.5422	16.3227	7.2306	4.5412
UDCP	2.2087	4.7651	0.6386	-52.541	0.4745	20.9495	6.6563	4.2017
NLD	1.3404	5.4064	0.6106	-86.497	0.5711	32.0813	7.3242	4.8201
MSCW	<u>4.3083</u>	<u>6.2134</u>	0.6945	-0.3386	0.5627	28.0830	7.3642	4.5821
DHDP	<u>4.3633</u>	6.0623	0.7086	<u>1.4060</u>	0.5778	<u>37.4275</u>	7.0837	5.6229
IBLA	3.8097	<u>6.2714</u>	0.5498	-0.2852	0.5686	32.7881	7.1234	4.6271
TSE	3.4320	5.7851	0.6662	-23.336	0.5334	22.4793	7.2983	4.6012
WSCT	2.2766	5.6662	0.6426	-60.083	0.5659	16.8319	7.5255	4.8475
UGAN	4.0091	5.6549	0.6278	<u>3.3558</u>	0.5700	20.8231	7.4872	5.1097
MDGAN	4.2464	5.7633	0.6625	<u>4.2245</u>	<u>0.5739</u>	27.9329	<u>7.7010</u>	<u>5.4499</u>
OURS	4.4722	6.2836	0.7209	1.3907	<u>0.5730</u>	<u>37.1664</u>	7.7090	<u>5.3860</u>

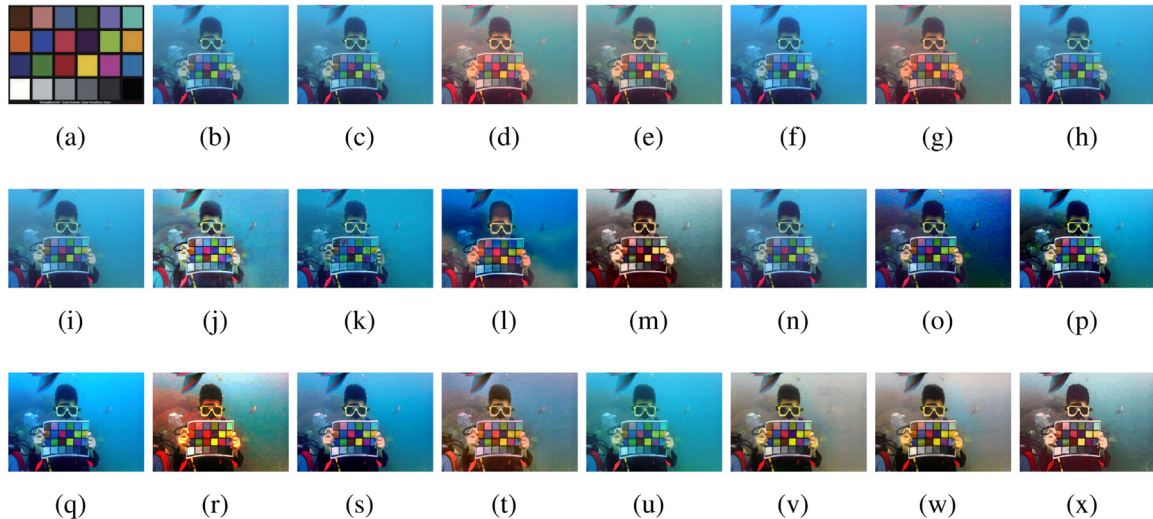


Fig. 13. Color accuracy test. (a) Ground truth, (b) Raw image, (c) MaxRGB, (d) Gray-World, (e) Shade-of-Gray, (f) Gray-Edge, (g) White-Balance, (h) White-Patch, (i) MSRCR, (j) CLAHE, (k) WCID, (l) VRE, (m) ARC, (n) UDCP, (o) NLD, (q) MSCW, (r) DHDP, (s) IBLA, (t) TSE, (u) WSCT, (v) UGAN, (w) MDGAN, (x) OURS. Best viewed with zoom-in.

WCID brings in color casts, such as the colors in the fourth row and second and third columns. VRE can remove the color cast, but color blur appears and color details are not unveiled in Fig. 13(m). UDCP, NLD, MSCW and IBLA have an ability to recover most colors, but fail in removing few color casts in the fourth row and second and third columns. Although DHDP shows the ability to remove the effect of color distortions, reddish deviation and undesirable artifacts are exhibited in Fig. 13(r). TSE, UGAN and MDGAN have positive effects on restoring the colors shown in Fig. 13(t), (v) and (w), but slight blurring can be seen in Fig. 13(v). The proposed method not only can remove the color casts of the Chart image, but also is capable of unveiling more color details in Fig. 13(x). The color accuracy test upholds the validity of the proposed method in restoring the color to the genuine color of ground truth. In addition, the robustness of the proposed method to different camera settings is demonstrated since the color is generally captured from various cameras. In Figs. 14 and 15, the proposed method is compared with the 22 approaches (add the SSR method) on two underwater images from Ancuti et al. (2012, 2018) that contain

the standard ColorChecker 24 X-Rite Chart respectively captured by the Olympus Tough 6000 and Canon D10 cameras. It is shown in Figs. 14(a) and 15(a) that various color casts are introduced by these professional cameras. Comparing Fig. 14(b)–(g) with Fig. 15(b)–(g), MaxRGB, Shade-of-Gray, Gray-Edge and White-Patch are lower robust to preserve the uniformity in color appearance for different cameras, while Gray-World and White-Balance have slight uniformity in color cast removal. For SSR and MSRCR, their results of color robustness to different cameras are presented poorly. VRE maintains the color consistency under different cameras, but its color details are blurred in Figs. 14(m) and 15(m). CLAHE exhibits preferable color robustness to different cameras, but undesirable artifacts are introduced in Figs. 14(j) and 15(j). FVR fails in the color uniformity for different cameras, serious artifacts and color spots emerge in Figs. 14(k) and 15(k). WCID, ARC, UDCP, NLD, MSCW and IBLA are poor to preserve the color uniformity in different cameras, although they are capable of removing most color casts. TSE has a disparity between the reference color and its restored color, as seen in Figs. 14(t) and 15(t). DHDP has a capacity to

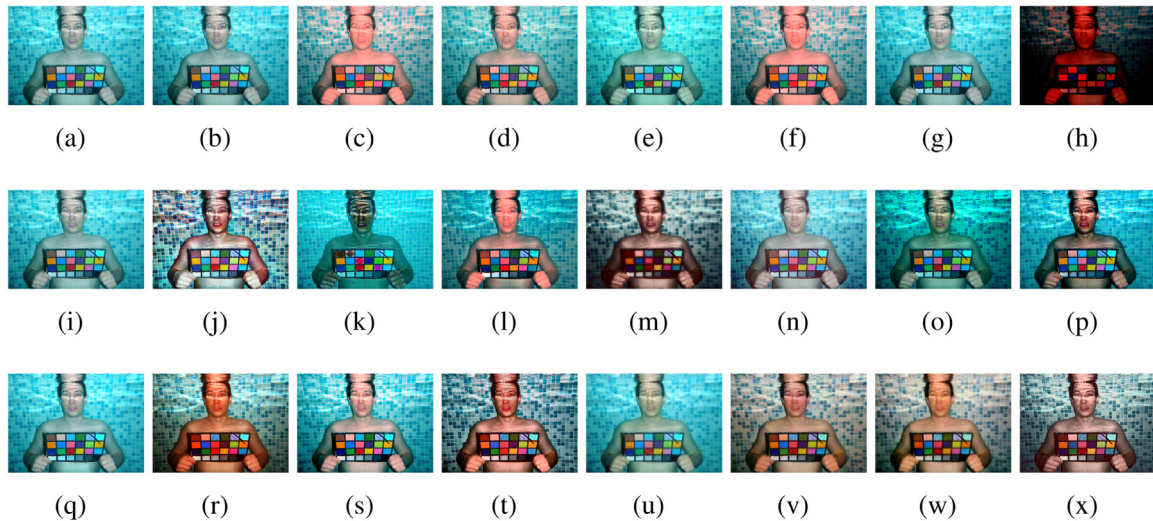


Fig. 14. Comparative results of different methods on an underwater image taken from the Olympus Tough 6000 camera. (a) Raw image, (b) MaxRGB, (c) Gray-World, (d) Shade-of-Gray, (e) Gray-Edge, (f) White-Balance, (g) White-Patch, (h) SSR, (i) MSRCR, (j) CLAHE, (k) FVR, (l) WCID, (m) VRE, (n) ARC, (o) UDCP, (p) NLD, (q) MSCW, (r) DHDHP, (s) IBLA, (t) TSE, (u) WSCT, (v) UGAN, (w) MDGAN, (x) OURS. Best viewed with zoom-in.

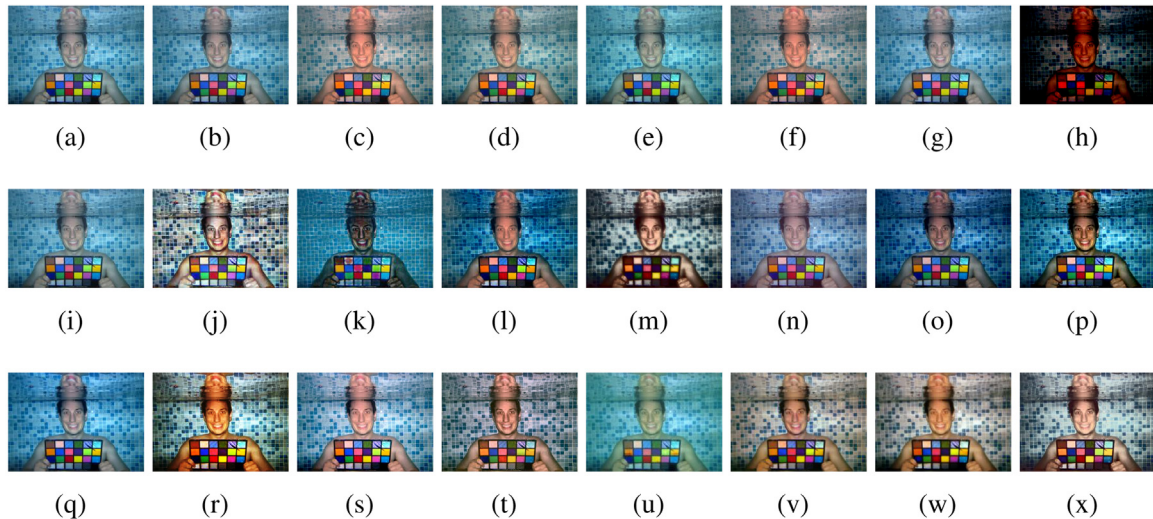


Fig. 15. Comparative results of different methods on an underwater image taken from the Canon D10 camera. (a) Raw image, (b) MaxRGB, (c) Gray-World, (d) Shade-of-Gray, (e) Gray-Edge, (f) White-Balance, (g) White-Patch, (h) SSR, (i) MSRCR, (j) CLAHE, (k) FVR, (l) WCID, (m) VRE, (n) ARC, (o) UDCP, (p) NLD, (q) MSCW, (r) DHDHP, (s) IBLA, (t) TSE, (u) WSCT, (v) UGAN, (w) MDGAN, (x) OURS. Best viewed with zoom-in.

remove color difference, but slight reddish deviations are observed in Figs. 14(r) and 15(r). UGAN and MDGAN eliminate the color dissimilarity from different cameras, while WSCT cannot be displayed in Figs. 14(u) and 15(u). Their blurred color details are illustrated in Figs. 14(u)–(w) and 15(u)–(w). As shown in Figs. 14(x) and 15(x), the proposed method has higher robustness in terms of maintaining color uniformity, recovering more color details, and removing undesirable artifacts.

4.6. Structural enhancement comparison

To verify the superiority of the proposed method on underwater structure enhancement, the proposed method is compared with the 22 methods on the four underwater images by measuring the number of restored visible edges in blind contrast enhancement assessment (Hautiere et al., 2011). In Table 2, the proposed method gains higher numbers of restored visible edges than other methods, and for the extremely deteriorated ‘Fish’ image, the proposed restored number is ranked to be the second-best, comparable to that of DHDHP. Fig. 16 provides partial results of visible edges restored by different methods on

the four underwater images, and one can see that more visible edges are restored in the proposed method. MaxRGB, Gray-World, Shade-of-Gray, Gray-Edge, White-Balance and White-Patch are unobvious in increasing the number of visible edges. The numbers of visible edges using SSR and MSRCR are lower and more structures cannot be recovered by MSRCR. VRE increases the number of visible edges by a variational retinex-based framework, but its structural improvement is confined due to that first-order gradient priors cannot recover more details. CLAHE obtains high numbers of visible edges and apparent structural enhancement, while its low number of visible edges are matched with poor structural promotion. FVR and WCID improve the numbers of restored structures, but unclear structures are seen in the extreme underwater image. ARC, UDCP, NLD, MSCW and IBLA have an ability to promote the numbers of restored structures, however, they are difficult to maintain the superiority of structural enhancement for the ‘Fish’ image. TSE, WSCT, UGAN and MDGAN have positive effects in increasing the numbers of visible edges, nevertheless, their structures are not promoted in the extreme underwater image. DHDHP improves the numbers of restored edges, but reddish casts and undesirable artifacts emerge in Fig. 10(r). Fortunately, the proposed method is capable

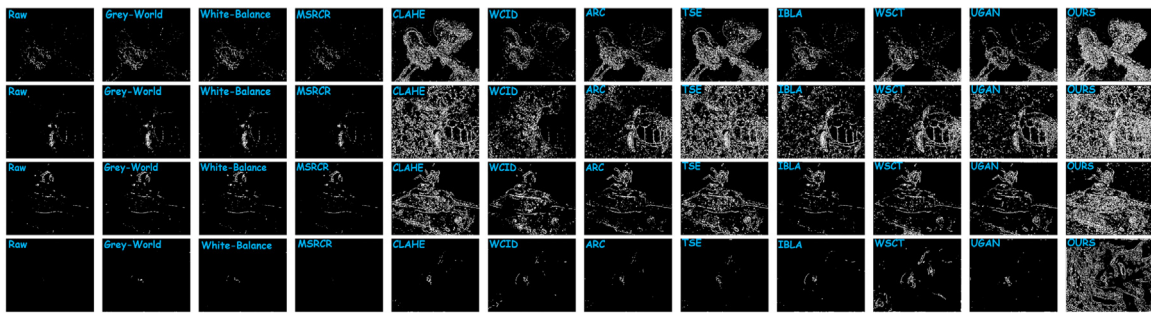


Fig. 16. Visible edges restored by different methods on four underwater images.

Table 2

The number of visible edges restored by different methods on four underwater images. (Red bold: best, green underline: second best, blue italic: third best).

Methods	Photographic	Turtle	Tank	Fish
Raw	2500	1963	2159	3216
MaxRGB	3617	2489	2418	3222
Gray-World	4485	2850	2740	3307
Shade-of-Gray	4245	2720	2575	3259
Gray-Edge	3142	2066	2137	3157
White-Balance	4471	2797	2728	3308
White-Patch	3545	2565	2413	3224
SSR	2315	1973	2873	3290
MSRCR	2510	2003	2967	3418
CLAHE	38437	56673	27137	3760
FVR	12377	18321	14176	3279
WCID	9007	19336	13954	3288
VRE	26687	58123	22202	41692
ARC	20979	24772	9456	3641
UDCP	33399	59567	<u>43862</u>	14883
NLD	<u>51177</u>	50975	27811	5640
MSCW	39014	57331	28242	5085
DHDP	39257	63415	25182	47125
IBLA	10975	29439	7292	3882
TSE	36141	<u>64909</u>	22202	3726
WSCT	13813	29712	12346	6082
UGAN	17271	29764	11893	3915
MDGAN	20515	41719	13109	9411
OURS	65132	94365	49686	<u>44046</u>

of restoring more visible edges, and outperforms other methods in the performance of structural enhancement. As shown in Fig. 11(b)(c) and Table 1, the proposed method yields the best UIQM and UIConM values, which confirms the validity of the proposed method in sharpness and contrast enhancement.

4.7. Challenging underwater scenes comparison

In addition to the above test on the 50 underwater images, the effectiveness of the proposed method is validated on challenging underwater images from Underwater Image Enhancement Benchmark Dataset (UIEBD) (Li et al., 2019). The first five lines of Fig. 17(a) considers extreme scenes in turbid water, where underwater images present yellowish due to strongly attenuated blue channels, and the rest five rows of Fig. 17(a) shows underwater scenes under deep water and low illumination conditions, where underwater images appear under-exposure and greenish due to limited and non-uniform illuminations. Fig. 17(b)–(h) shows the enhanced results using different methods on these challenging underwater images. From these enhanced images in turbid water, it is observed that ARC, UDCP, and TSE fail in restoring original colors, and cannot remove the disturbed yellow layer and improve underwater structural contrast. IBLA achieves slightly better structures but cannot eliminate the interference of the turbid color. VRE can clean the yellowish layer and promote the contrast of image structures, but its results are slightly over-enhanced with unnatural colors. DHDP and the proposed method not only recover natural color

but also raise image contrast, and in particular, the proposed method yields better results of detail enhancement. From the enhanced results of limited and non-uniform illuminations, one can observe that ARC is limited in color correction and structural enhancement, and its over-reddish results appear in the enhanced image of non-uniform illumination, as seen in the last row of Fig. 17(c). Although UDCP can improve contrast to a certain extent, its color is overall dark and cannot be naturally restored, and this method fails in enhancing the underwater image of non-uniform illumination shown in the last row of Fig. 17(d). The effect of color correction and contrast improvement is positive in IBLA, but shown in the sixth and eighth rows of Fig. 17(f), this method has an obvious reddish color shift. The under-enhanced results of color recovery and structure improvement are shown in the enhanced images of TSE, and blurring details are observed in VRE. By contrast, DHDP and the proposed method are capable of robustly removing color casts and obviously promoting image contrast when enhancing underwater images with limited and non-uniform illuminations. Furthermore, clearer detail structures can be found in the proposed method, and the proposed method is more robust to above challenging scenes.

4.8. Ablation study and comparison with Zhuang and Ding (2020)

To demonstrate the effect of each component in the proposed model, an ablation investigation is performed on the previously-used four underwater images, involving the following experiments: (1) the proposed model (Ours), (2) the proposed model without illumination adjustment (Our retinex model), (3) the proposed model without Bayesian retinex enhancement and illumination adjustment (Our color correction). The enhanced images are visually presented in Fig. 18(a)–(d), and the quantitative evaluations of UIQM and UCIQE are reported in Fig. 18(e) and (f). It is noted in Fig. 18(b) that our color correction can remove the color casts of raw underwater images, and improve UIQM and UCIQE in Fig. 18(e) and (f). Our retinex model acquires observable color restoration and boosts remarkable contrast in Fig. 18(c), and the UIQM and UCIQE are further promoted in Fig. 18(e) and (f). As seen in Fig. 18(d), the proposed model shows an ability to reveal more details of both color correction and contrast promotion, and outperforms our retinex model and our color correction. Meanwhile, the proposed model gains the highest UIQM and UCIQE, as exhibited in Fig. 18(e) and (f), which illustrates the positive effect of each component in the proposed model. To sum up, our color correction aims to correct color casts, and our Bayesian retinex enhancement model is effective in contrast boost and color restoration, then the illumination adjustment is further to restore more details of color and structure.

In addition, the proposed method is compared with the edge-preserving filtering Retinex method (EPF) (Zhuang and Ding, 2020) in Fig. 19. It is noted that compared with the EPF method, the proposed method achieves higher UIQM and UCIQE and yields better results of color correction and structure improvement. The better performance benefits from the proposed Bayesian retinex model with multiorder gradient priors of reflectance and illumination and accurate norm constraints.

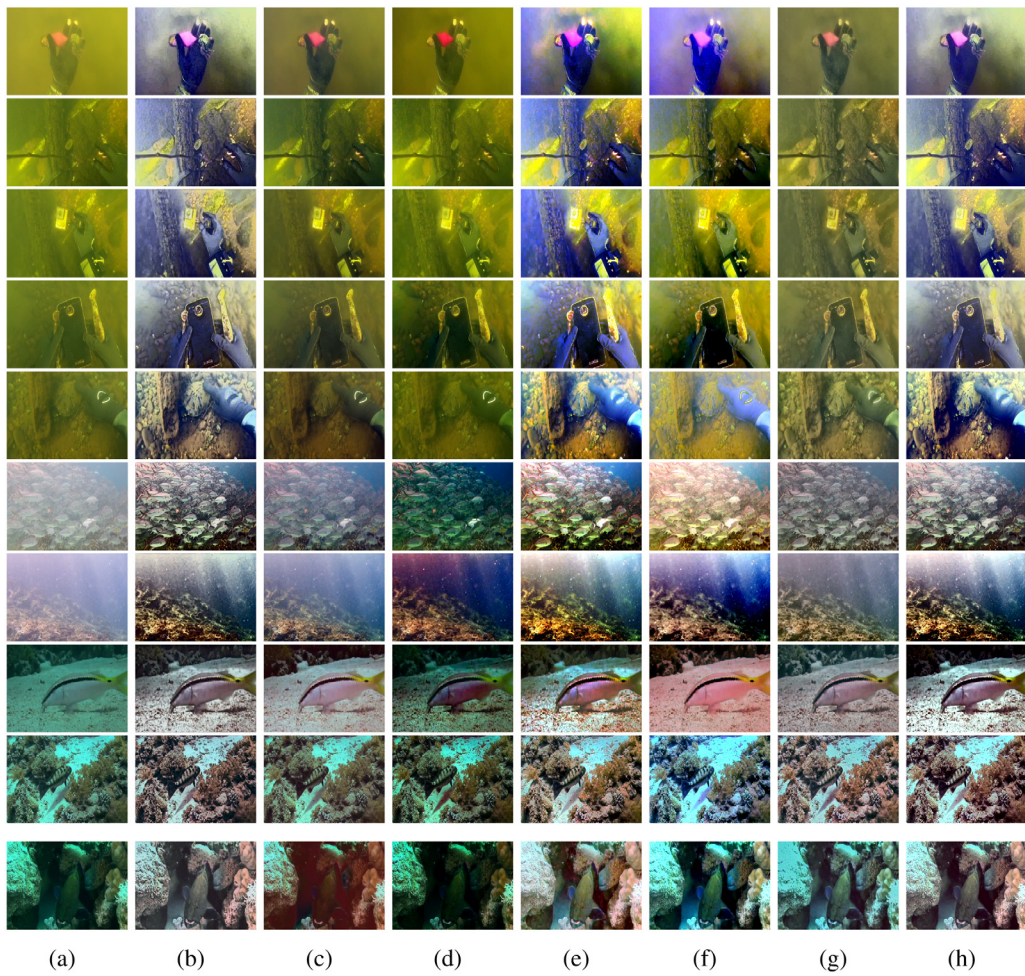


Fig. 17. Enhancement results of different methods on challenging underwater images from the dataset UIEBD. (a) Raw image, (b) VRE, (c) ARC, (d) UDCP, (e) DHDP, (f) IBLA, (g) TSE, (h) OURS. Best viewed with zoom-in.

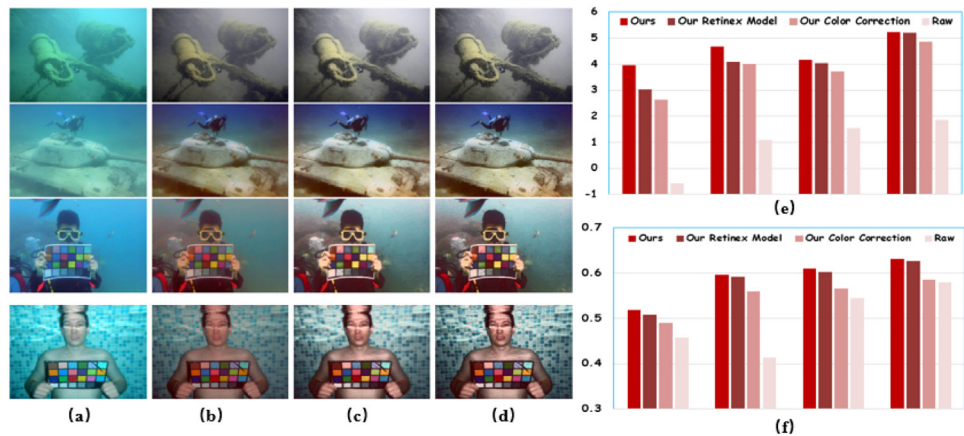


Fig. 18. Ablation study of the proposed method. (a) Raw image, (b) Our color correction, (c) Our retinex model, (d) Ours. (e) UIQM of (a)–(d), (f) UCIQE of (a)–(d).

4.9. Parameter evaluation

The impact of regularization parameters on the proposed method is evaluated. The effect of parameters v_1, v_2, v_3, v_4 in the model (10) is first investigated, and Fig. 20(a)–(d) plot the curves of UIQM versus the four parameters v_1, v_2, v_3, v_4 on the underwater image 'Tank', where their corresponding illumination and reflectance are attached below. From Fig. 20(a), one can see that when v_1 varies from 0.01 to 100, the tendency of UIQM first slightly increases and then degrades, and the

best UIQM is gained when v_1 reaches 1. In Fig. 20(b) and (c), UIQM first stabilizes and then decreases when v_2 increases from $1e-5$ to $1e-1$ or v_3 grows from $1e-7$ to $1e-3$. It is seen that the critical UIQM variation emerges when v_2 and v_3 are $1e-3$ and $1e-4$, respectively. As can be seen in Fig. 20(d), UIQM is improved when v_4 increases to $1e-3$, but its result declines when v_4 is larger than $1e-3$, and note that UIQM is best when v_4 is $1e-3$. Then the effect of parameters λ_1 and λ_2 in the model (11) is assessed, and their curves are respectively plotted in Fig. 20(e) and (f). The variations of λ_1 and λ_2 are respectively similar to those of

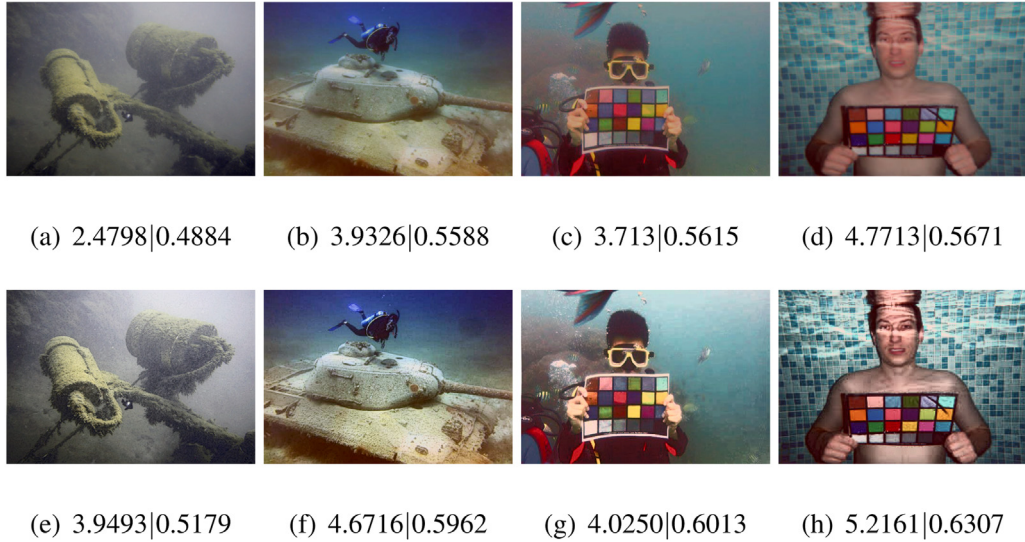


Fig. 19. Comparison results of the proposed method and the EPF method. The metric scores (UIQM|UCIQE) are reported below enhanced images by the EPF method (a)–(d) and the proposed method (e)–(h).

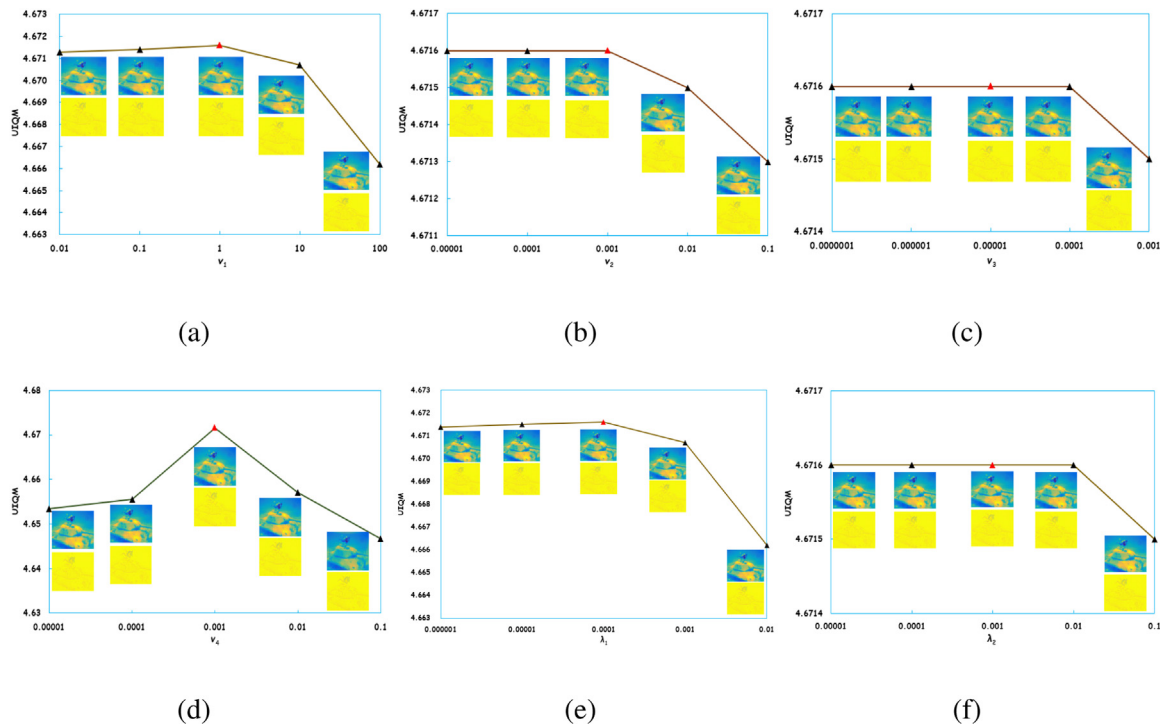


Fig. 20. Parameter evaluation. (a) UIQM versus v_1 , (b) UIQM versus v_2 , (c) UIQM versus v_3 , (d) UIQM versus v_4 , (e) UIQM versus λ_1 , (f) UIQM versus λ_2 .

v_1 and v_3 , and their settings $\lambda_1 = 1e-4$ and $\lambda_2 = 1e-3$ are empirically suitable for the better UIQM. It is worth noting that despite the changes of these parameters, UIQM has a maximum change value 0.0054 and a minimum change value 0.0001, demonstrating very small changes of UIQM. Through comparing corresponding illumination and reflectance, it is found that the changes for their illumination and reflectance are almost insignificant as these parameters change. The aforementioned results validate the rationality of the parameter settings mentioned earlier for decent results, and they demonstrate the robustness of the proposed method to the variation of these parameters.

4.10. Convergence analysis and computation complexity

The convergence of the proposed optimization algorithm is analyzed in this experiment where two underwater images with different sizes of 412×550 and 2112×2816 are tested respectively. Fig. 21 plots the relationship curves between the errors $\epsilon_I (\|I^k - I^{k-1}\|/\|I^{k-1}\|)$, $\epsilon_R (\|R^k - R^{k-1}\|/\|R^{k-1}\|)$ and the number of iterations (k), and it presents an intuitive illustration of the convergence speed of the proposed method. From the curves of Fig. 21, it is observed that the convergence rate is fast and independent of image size, and the errors ϵ_I , ϵ_R become

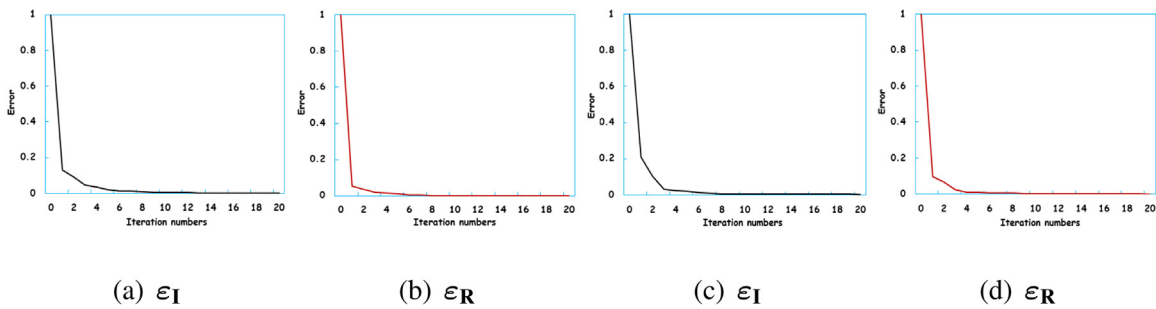


Fig. 21. The relation between the error (ϵ_I , ϵ_R) and the iteration numbers (k). (a)(b) image with the size of 412×550 , (c)(d) image with the size of 2112×2816 .

Table 3
The keypoint number of ARC, IBLA and the proposed method on four underwater images.

	Raw	ARC	IBLA	OURS
Photographic	20	27	19	69
Turtle	72	208	217	462
Tank	33	60	70	235
Fish	7	45	45	168

smaller as the iteration number k increases. For all test images, the proposed algorithm stably converges when reaching 8 iterations, which is suitable to be the maximum number of iterations (T) sufficient to generate decent results in the experiments. This convergence phenomenon is due to the proposed optimization algorithm which can split the complex energy minimization problem into a couple of simple sub-problems for optimizing \mathbf{R} and \mathbf{I} efficiently and separately.

For processing an underwater image with the size of 412×550 , the proposed approach takes about 0.14 seconds (s), which outperforms the three deep learning-based methods WSCT (0.88 s), UGAN (0.32 s) and MDGAN (0.52 s), and the proposed method runs faster than other methods including TSE (0.72 s), IBLA (42.37 s), DHDPP (1.46 s), MSCW (1.09 s), NLD (1.68 s), UDCP (29.97 s), ARC (0.29 s), WCID (1.59 s), FVR (2.05 s), MSRCR (0.42 s) and Gray-Edge (0.18 s). It should be noted that the three deep learning-based methods require more than 10 hours on their training time. MaxRGB, Gray-World, Shade-of-Gray, White-Balance, White-Patch, SSR, CLAHE and VRE require about 0.05, 0.08, 0.09, 0.02, 0.03, 0.13, 0.05 and 0.12 seconds respectively, although the proposed method takes more runtime, the proposed enhancement results are better in terms of qualitative and quantitative results. It is worth mentioning that the Matlab code of the proposed method is unoptimized, and it can be further optimized and accelerated by adopting C/C++ programming and Graphics Processing Units (GPUs).

4.11. Application tests

The proposed technique is found to be suitable for several applications such as underwater keypoint detection, underwater saliency detection, underwater depth map estimation, and underwater image segmentation. For the four tests, different enhancement methods are first used to enhance raw underwater images, and then different post-processing operations for these applications are respectively performed on raw and enhanced underwater images.

Underwater keypoint detection. The number of the keypoints in the SIFT (Lowe, 2004) is counted on the four raw underwater images and the enhanced images using ARC, IBLA and the proposed method. It is observed from Fig. 22(b) and (c) that ARC and IBLA obtain relatively more keypoints than raw underwater images in most cases, and their quantitative results are reported in Table 3. It is noted that the proposed method yields highest keypoint numbers in Table 3, and in Fig. 22(d) the proposed results visually overwhelms ARC and IBLA. These promising results demonstrate that the proposed method has an

ability to restore more crucial features of underwater images, which is more beneficial to underwater object detection and recognition.

Underwater saliency detection. The detection of underwater saliency is to make underwater objects stand out relative to their neighbors and capture our attention, which is helpful for underwater image segmentation, underwater object recognition, underwater image compression, to name a few. To detect underwater saliency of the four raw images and the enhanced results using IBLA, ARC and the proposed method, a graph-based manifold ranking method (Yang et al., 2013) is employed, which has the advantages of higher precision and faster speed. In Fig. 23, one can see that the proposed saliency maps retain more accurate contents of salient objects compared with other approaches, and it is noticeable that better boundaries of salient targets are preserved by using the proposed technique. These experimental results confirm that the proposed technique performs better underwater saliency detection when against other methods.

Underwater depth map estimation. The estimation of underwater depth map is an important step for underwater scene reconstruction and restoration. To equivalently estimate underwater image depth, a transmission estimation way (Berman et al., 2016) is adopted to represent depth maps of raw and enhanced underwater images. It is seen from Fig. 24 that the proposed depth maps contain more refined and accurate contents than those of IBLA, ARC, and Raw, in particular, this superiority in the areas of boundaries and foreground objects are more prominent. This test shows that the proposed approach is more effective in high quality of underwater depth estimation.

Underwater image segmentation. The aim of underwater image segmentation is to divide an image into several disjoint and homogeneous regions with respect to some specific and unique properties. A superpixel-based fast FCM clustering algorithm (Lei et al., 2019) is used due to its fast and robust color image segmentation, and it is adopted on the raw underwater images and the enhanced results of ARC, IBLA and the proposed method. It is clear in Fig. 25 that compared with the segmentation results using raw, ARC and IBLA, the proposed segmentation images are more consistent and accurate, especially in the places of foreground objects and segmentation boundaries. This task supports that the proposed technique provides better segmentation results for underwater image segmentation.

5. Conclusion

This paper has proposed a Bayesian retinex method for single underwater image enhancement with multiorder gradient priors of reflectance and illumination. Experimental results demonstrate the robust and decent performance of the proposed method. The advantages of the proposed method are summarized below: (1) A simple but effective color correction approach is used to remove color castes and restore naturalness, which is an efficient color preprocess for other underwater enhancement methods. (2) A Bayesian retinex enhancement model is established with multiorder gradient priors of reflectance and illumination, along with imposing l_1 and l_2 norms on reflectance and illumination respectively. The multiorder gradient priors can capture

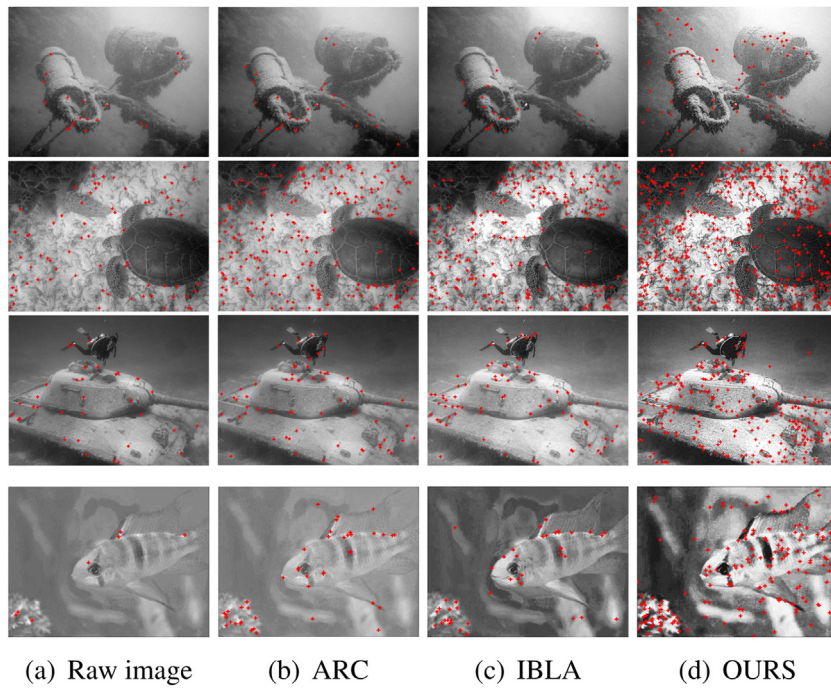


Fig. 22. Underwater keypoint detection.

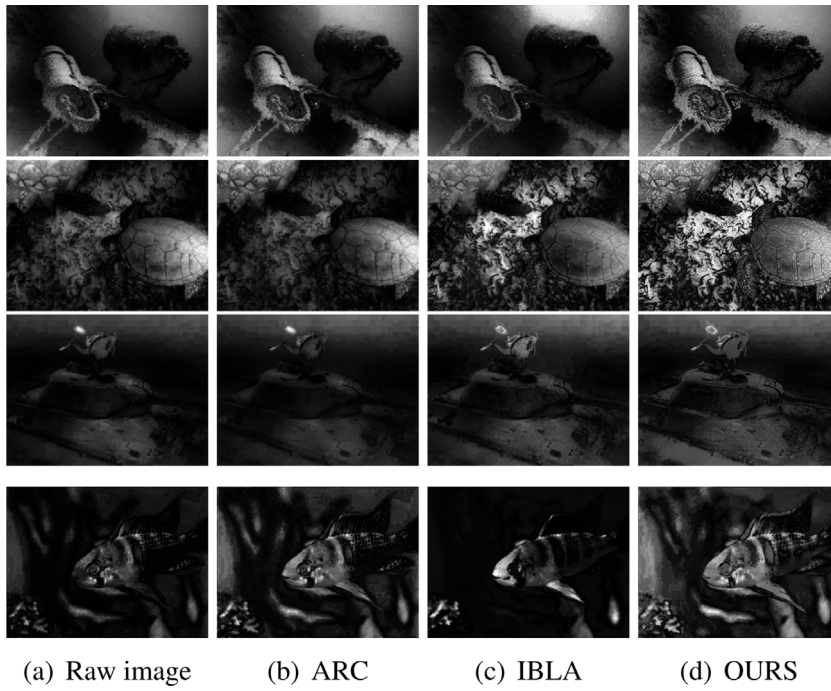


Fig. 23. Underwater saliency detection.

more fine-scale and complete structures by modeling spatial smoothness and linear approximations on both reflectance and illumination, and appropriate norms are adopted to model them according to above observations for different sparse characteristics. The proposed prior is a new prior for solving image enhancement and restoration problems by making effective and comprehensive use of first-order and second-order gradient priors. (3) A complex underwater image enhancement problem is decomposed into two simple denoising subproblems where their mathematical convergence can be analyzed, and then an efficient

alternating optimization algorithm is derived to arrive at their solutions. The sub-problem decomposition and corresponding alternating optimization are an effective scheme to address complex optimization objective functions. (4) The proposed model is straightforwardly performed on the pixel-wise operations without requiring extra prior of underwater imaging conditions. (5) The comprehensive analyses show the effective performance of the proposed method in terms of color accuracy, challenging underwater scenes, ablation study, parameter evaluation, and algorithm convergence.

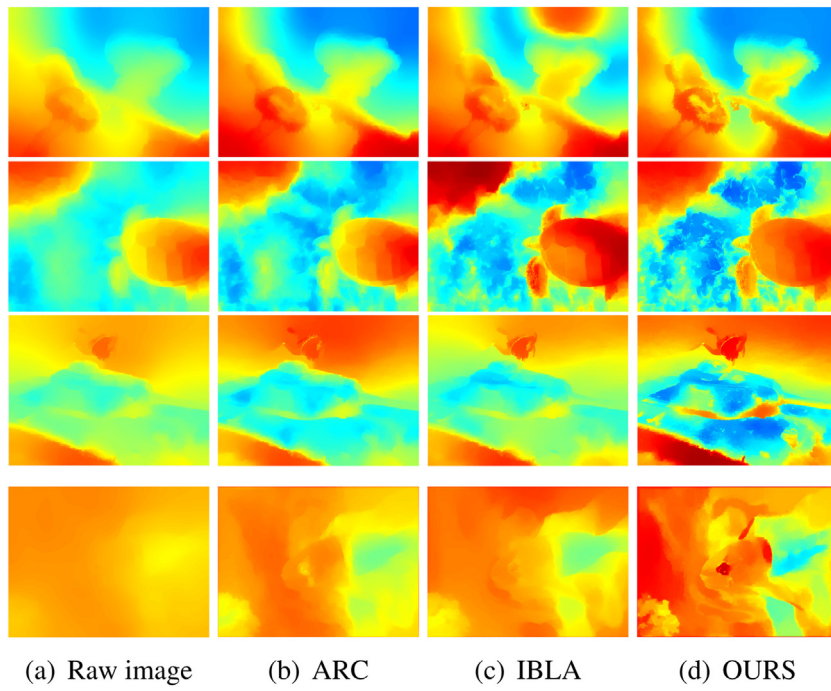


Fig. 24. Underwater depth map estimation.

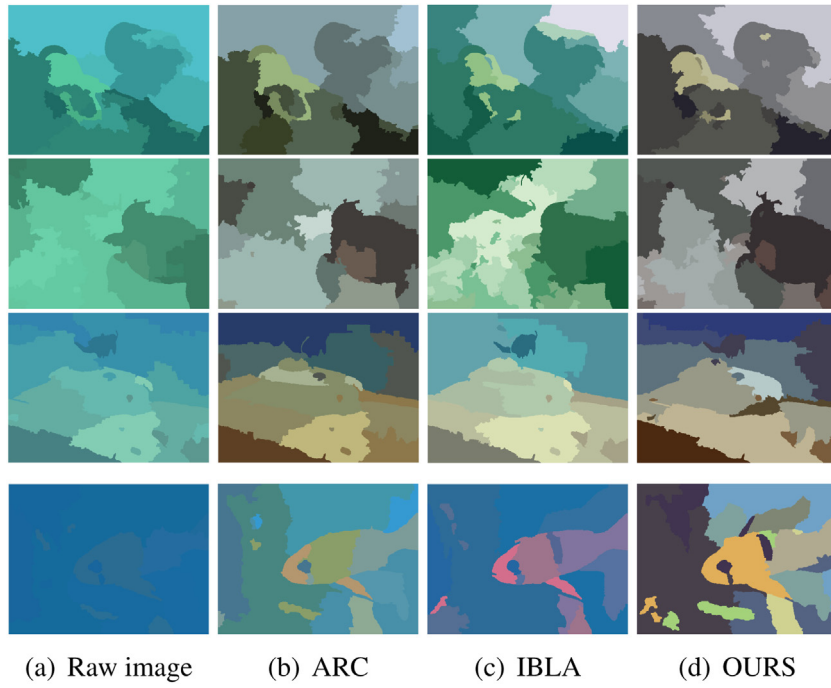


Fig. 25. Underwater image segmentation.

In the future, the runtime of the proposed method will be shortened by optimizing and accelerating the code, in particular, C/C++ programming and Graphics Processing Units (GPUs) can be adopted to reduce the main runtime of the proposed algorithm which is spent on solving alternating subproblems. The applicability of the proposed prior will be expansively investigated to combine with other optimization techniques (Khatir and Wahab, 2019; Khatir et al., 2019b; Tran-Ngoc et al., 2018; Tiachacht et al., 2018) for image enhancement and restoration. Furthermore, under the proposed Bayesian framework, a better fusion of the proposed prior and other deep learning-based techniques (Tran-Ngoc et al., 2019; Khatir et al., 2019a; Nguyen et al., 2019; Wang et al.,

2021) will be designed to improve the performance of low-level vision tasks and then better serve high-level vision tasks in computer vision.

CRediT authorship contribution statement

Peixian Zhuang: Conceptualization, Methodology, Software, Validation, Data curation, Writing - original draft, Writing - review & editing, Visualization. **Chongyi Li:** Methodology, Formal analysis, Writing - review & editing. **Jiamin Wu:** Supervision, Project administration, Funding acquisition.

Declaration of competing interest

The authors declare that they have no known competing financial interests or personal relationships that could have appeared to influence the work reported in this paper.

Acknowledgments

The authors would like to thank the anonymous reviewers for their valuable and helpful comments. **Peixian zhuang** is writing original draft, including conceptualization, methodology, software, validation, data processing and visualization, and he is writing the response of the reviews' comment and editing the revised manuscript. **Chongyi Li** and **Jiamin Wu** polish the revised manuscript and provide helpful suggestions on experimental and mathematical analysis. This work was supported in part by the National Natural Science Foundation of China under Grants 61701245, 62071272, the National Key Research and Development Program of China under Grants 2020AAA0130000.

Appendix

In this appendix, the existence for the solution to the minimization problem (10) is first proved, and an analysis of the convergence of corresponding subproblems is provided subsequently.

A.1. Existence for solution of (10)

Thanks to the literatures (Fu et al., 2015; Ng and Wang, 2011), a proof of the existence for the solution of (10) is provided. For simplicity, the following set is defined:

$$\Lambda = \{(\mathbf{I}, \mathbf{R}) | (\mathbf{I}, \mathbf{R}) \in \mathbf{W}^{2,2}(\Omega) \times \mathbf{W}^{2,1}(\Omega), \mathbf{L} \leq \mathbf{I}\} \quad (21)$$

The associated energy minimization problem is

$$\begin{aligned} \min_{(\mathbf{I}, \mathbf{R}) \in \Lambda} E(\mathbf{I}, \mathbf{R}) = & \|\mathbf{I} \cdot \mathbf{R} - \mathbf{L}\|_2^2 + v_1 \|\nabla \mathbf{R}\|_1 + v_2 \|\Delta \mathbf{R}\|_1 \\ & + v_3 \|\nabla \mathbf{I}\|_2^2 + v_4 \|\Delta \mathbf{I}\|_2^2 \quad \text{s.t. } \mathbf{L} \leq \mathbf{I} \end{aligned} \quad (22)$$

Theorem 1. Let $\mathbf{L} \in L^\infty(\Omega)$, the problem (22) has at least one solution.

Proof. The energy $E(\mathbf{I}, \mathbf{R})$ will be finite if \mathbf{I} and \mathbf{R} are two constants. Suppose $(\mathbf{I}^k, \mathbf{R}^k) \subset \Lambda$ is a minimizing sequence of problem (22), there exists a positive constant M such that

$$E(\mathbf{I}^k, \mathbf{R}^k) \leq M \quad (23)$$

The above inequality can be rewritten as

$$\begin{aligned} & \|\mathbf{I}^k \cdot \mathbf{R}^k - \mathbf{L}\|_2^2 + v_1 \|\nabla \mathbf{R}^k\|_1 + v_2 \|\Delta \mathbf{R}^k\|_1 \\ & + v_3 \|\nabla \mathbf{I}^k\|_2^2 + v_4 \|\Delta \mathbf{I}^k\|_2^2 \leq M \end{aligned} \quad (24)$$

The boundedness of $\|\nabla \mathbf{I}^k\|_2^2$ and $\|\Delta \mathbf{I}^k\|_2^2$ guarantees that $\{\mathbf{I}^k\}$ is uniformly bounded in $\mathbf{W}^{2,2}(\Omega)$. Note that $\mathbf{W}^{2,2}(\Omega)$ is embedded in $L^2(\Omega)$, and up to a subsequence, $\{\mathbf{I}^k\}$ converges to $\mathbf{I}^* \in \mathbf{W}^{2,2}(\Omega)$, i.e.,

$$\mathbf{I}^k \in L^2(\Omega) \longrightarrow \mathbf{I}^* \text{ and } \mathbf{I}^k \rightharpoonup \mathbf{I}^* \in \mathbf{W}^{2,2}(\Omega) \quad (25)$$

Similar to the related proof in the literatures (Fu et al., 2015), the boundedness of $\|\nabla \mathbf{R}^k\|_1$ and $\|\Delta \mathbf{R}^k\|_1$ guarantees that $\{\mathbf{R}^k\}$ is uniformly bounded in $\mathbf{W}^{2,1}(\Omega)$. Note that $\mathbf{W}^{2,1}(\Omega)$ is embedded in $L^1(\Omega)$, and up to a subsequence, $\{\mathbf{R}^k\}$ converges to $\mathbf{R}^* \in \mathbf{W}^{2,1}(\Omega)$, i.e.,

$$\mathbf{R}^k \in L^1(\Omega) \longrightarrow \mathbf{R}^* \text{ and } \mathbf{R}^k \rightharpoonup \mathbf{R}^* \in \mathbf{W}^{2,1}(\Omega) \quad (26)$$

Note that (25) holds for \mathbf{I}^k , which corresponds to \mathbf{R}^k . And (26) holds for \mathbf{R}^k , which corresponds to \mathbf{I}^k . Thus it is deduced that, up to a

subsequence, $\{(\mathbf{I}^k, \mathbf{R}^k)\}$ satisfies both (25) and (26). As a consequence of the lower semicontinuity for the $\mathbf{W}^{2,2}(\Omega)$ and $\mathbf{W}^{2,1}(\Omega)$ norms,

$$\begin{aligned} \liminf_{k \rightarrow \infty} (v_3 \|\nabla \mathbf{I}^k\|_2^2 + v_4 \|\Delta \mathbf{I}^k\|_2^2) & \geq v_3 \|\nabla \mathbf{I}^*\|_2^2 + v_4 \|\Delta \mathbf{I}^*\|_2^2 \\ \liminf_{k \rightarrow \infty} (v_1 \|\nabla \mathbf{R}^k\|_1 + v_2 \|\Delta \mathbf{R}^k\|_1) & \geq v_1 \|\nabla \mathbf{R}^*\|_1 + v_2 \|\Delta \mathbf{R}^*\|_1 \end{aligned} \quad (27)$$

Since $\mathbf{I}^k \cdot \mathbf{R}^k \rightharpoonup \mathbf{I}^* \cdot \mathbf{R}^*$ in $L^2(\Omega)$ and recalling the lower semicontinuity for the $L^2(\Omega)$ norm, it is derived that

$$\liminf_{k \rightarrow \infty} \|\mathbf{I}^k \cdot \mathbf{R}^k - \mathbf{L}\|_2^2 \geq \|\mathbf{I}^* \cdot \mathbf{R}^* - \mathbf{L}\|_2^2 \quad (28)$$

Therefore,

$$\min_{(\mathbf{I}, \mathbf{R}) \in \Lambda} E(\mathbf{I}, \mathbf{R}) = \liminf_{k \rightarrow \infty} E(\mathbf{I}^k, \mathbf{R}^k) \geq E(\mathbf{I}^*, \mathbf{R}^*) \quad (29)$$

meanwhile, $\mathbf{I}^* \geq \mathbf{L}$. The proof is completed.

A.2. Analysis for convergence of subproblems

Thanks to the literatures (Chan et al., 2015; Wu and Tai, 2011), a convergence analysis of corresponding subproblems is provided. The complex problem (10) can be transformed into two simple denoising subproblems:

Given \mathbf{I} , compute \mathbf{R} by solving

$$\min_{\mathbf{R}} E_1(\mathbf{R}) = \|\mathbf{I} \cdot \mathbf{R} - \mathbf{L}\|_2^2 + v_1 \|\nabla \mathbf{R}\|_1 + v_2 \|\Delta \mathbf{R}\|_1 \quad (30)$$

Given \mathbf{R} , compute \mathbf{I} by solving

$$\min_{\mathbf{I}} E_2(\mathbf{I}) = \|\mathbf{I} \cdot \mathbf{R} - \mathbf{L}\|_2^2 + v_3 \|\nabla \mathbf{I}\|_2^2 + v_4 \|\Delta \mathbf{I}\|_2^2 \quad \text{s.t. } \mathbf{L} \leq \mathbf{I} \quad (31)$$

It is attempted to prove the convergence of the two subproblems (30) and (31) respectively. Note that since (31) is a least square problem, a closed-form solution (18) can be easily deduced by taking the operations of derivative, least square and fast Fourier transform, and a constraint can be solved via a correction of numerical comparison. To prove the convergence of (30) is the key problem. As mentioned above, two auxiliary variables \mathbf{d} and \mathbf{h} are introduced into (30), and this problem is reformulated to be

$$\begin{aligned} \min_{(\mathbf{R}, \mathbf{d}, \mathbf{h})} & \|\mathbf{I} \cdot \mathbf{R} - \mathbf{L}\|_2^2 + v_1 \|\mathbf{d}\|_1 + v_2 \|\mathbf{h}\|_1 \\ & \text{s.t. } \mathbf{d} = \nabla \mathbf{R}, \mathbf{h} = \Delta \mathbf{R} \end{aligned} \quad (32)$$

To solve the constrained problem (32), the following augmented Lagrangian functional is derived with previously defined Lagrange multipliers \mathbf{m} and \mathbf{n} :

$$\begin{aligned} L(\mathbf{R}, \mathbf{d}, \mathbf{h}; \mathbf{m}, \mathbf{n}) = & \|\mathbf{I} \cdot \mathbf{R} - \mathbf{L}\|_2^2 + v_1 (\|\mathbf{d}\|_1 + \langle \mathbf{m}, \mathbf{d} - \nabla \mathbf{R} \rangle) \\ & + \frac{1}{2} \|\mathbf{d} - \nabla \mathbf{R}\|_2^2 + v_2 (\|\mathbf{h}\|_1 + \langle \mathbf{n}, \mathbf{h} - \Delta \mathbf{R} \rangle) \\ & + \frac{1}{2} \|\mathbf{h} - \Delta \mathbf{R}\|_2^2 \end{aligned} \quad (33)$$

According to Wu and Tai (2011, 2010), one of the saddle points of the augmented Lagrangian functional (33) corresponds to the minimizers of the problem (32). The (P2) problem in the proposed numerical algorithm can be equivalent to

$$\begin{aligned} (\mathbf{R}^{k+1}, \mathbf{d}^{k+1}, \mathbf{h}^{k+1}) &= \min_{(\mathbf{R}, \mathbf{d}, \mathbf{h})} L(\mathbf{R}, \mathbf{d}, \mathbf{h}; \mathbf{m}^k, \mathbf{n}^k) \\ \mathbf{m}^{k+1} &= \mathbf{m}^k + \mathbf{d}^{k+1} - \nabla \mathbf{R}^{k+1} \\ \mathbf{n}^{k+1} &= \mathbf{n}^k + \mathbf{h}^{k+1} - \Delta \mathbf{R}^{k+1} \end{aligned} \quad (34)$$

The convergence theory in Wu and Tai (2011) can be adopted to prove the convergence of (34) with $T \rightarrow \infty$ and $T = 1$ in Algorithm 1 respectively. The problem (30) has minimizers according to the convex analysis theory (Hiriart-Urruty and Lemarechal, 1996).

Theorem 2. Assume $(\mathbf{R}^*, \mathbf{d}^*, \mathbf{h}^*; \mathbf{m}^*, \mathbf{n}^*)$ be a saddle point of $L(\mathbf{R}, \mathbf{d}, \mathbf{h}; \mathbf{m}, \mathbf{n})$. Suppose that the problem (34) is exactly solved in each iteration, i.e. $T \rightarrow \infty$ in Algorithm 1. Then the sequence $(\mathbf{R}^k, \mathbf{d}^k, \mathbf{h}^k; \mathbf{m}^k, \mathbf{n}^k)$ satisfies

$$\left\{ \begin{array}{l} \lim_{k \rightarrow \infty} v_1 \|\mathbf{d}^k\|_1 + v_2 \|\mathbf{h}^k\|_1 + \|\mathbf{I} \cdot \mathbf{R}^k - \mathbf{L}\|_2^2 = E_1(\mathbf{R}^*) \\ \lim_{k \rightarrow \infty} \|\mathbf{d}^k - \nabla \mathbf{R}^k\|_2 = 0 \\ \lim_{k \rightarrow \infty} \|\mathbf{h}^k - \Delta \mathbf{R}^k\|_2 = 0 \\ \lim_{k \rightarrow \infty} \|\mathbf{I} \cdot (\mathbf{R}^k - \mathbf{R}^*)\|_2 = 0 \end{array} \right. \quad (35)$$

And (35) indicates that $\{\mathbf{R}^k\}$ is a minimizing sequence of $E_1(\cdot)$. If the minimizer of $E_1(\cdot)$ is unique, then $\mathbf{R}^k \rightarrow \mathbf{R}^*$.

Proof. $\bar{\mathbf{R}}^k, \bar{\mathbf{d}}^k, \bar{\mathbf{h}}^k, \bar{\mathbf{m}}^k$ and $\bar{\mathbf{n}}^k$ are defined as

$$\left\{ \begin{array}{l} \bar{\mathbf{R}}^k = \mathbf{R}^k - \mathbf{R}^* \\ \bar{\mathbf{d}}^k = \mathbf{d}^k - \mathbf{d}^* \\ \bar{\mathbf{h}}^k = \mathbf{h}^k - \mathbf{h}^* \\ \bar{\mathbf{m}}^k = \mathbf{m}^k - \mathbf{m}^* \\ \bar{\mathbf{n}}^k = \mathbf{n}^k - \mathbf{n}^* \end{array} \right. \quad (36)$$

Since $(\mathbf{R}^*, \mathbf{d}^*, \mathbf{h}^*; \mathbf{m}^*, \mathbf{n}^*)$ is a saddle point of $L(\mathbf{R}, \mathbf{d}, \mathbf{h}; \mathbf{m}, \mathbf{n})$, it is deduced that

$$L(\mathbf{R}^*, \mathbf{d}^*, \mathbf{h}^*; \mathbf{m}, \mathbf{n}) \leq L(\mathbf{R}^*, \mathbf{d}^*, \mathbf{h}^*; \mathbf{m}^*, \mathbf{n}^*) \leq L(\mathbf{R}, \mathbf{d}, \mathbf{h}; \mathbf{m}^*, \mathbf{n}^*) \quad (37)$$

and $\mathbf{d}^* = \nabla \mathbf{R}^*$, $\mathbf{h}^* = \Delta \mathbf{R}^*$. Together with (34), this relationship indicates

$$\left\{ \begin{array}{l} \bar{\mathbf{m}}^{k+1} = \bar{\mathbf{m}}^k + \bar{\mathbf{d}}^{k+1} - \nabla \bar{\mathbf{R}}^{k+1} \\ \bar{\mathbf{n}}^{k+1} = \bar{\mathbf{n}}^k + \bar{\mathbf{h}}^{k+1} - \Delta \bar{\mathbf{R}}^{k+1} \end{array} \right. \quad (38)$$

It follows that

$$\begin{aligned} & (v_1 \|\bar{\mathbf{m}}^k\|_2^2 + v_2 \|\bar{\mathbf{n}}^k\|_2^2) - (v_1 \|\bar{\mathbf{m}}^{k+1}\|_2^2 + v_2 \|\bar{\mathbf{n}}^{k+1}\|_2^2) \\ &= -2v_1 \langle \bar{\mathbf{m}}^k, \bar{\mathbf{d}}^{k+1} - \nabla \bar{\mathbf{R}}^{k+1} \rangle - v_1 \|\bar{\mathbf{d}}^{k+1} - \nabla \bar{\mathbf{R}}^{k+1}\|_2^2 \\ &\quad - 2v_2 \langle \bar{\mathbf{n}}^k, \bar{\mathbf{h}}^{k+1} - \Delta \bar{\mathbf{R}}^{k+1} \rangle - v_2 \|\bar{\mathbf{h}}^{k+1} - \Delta \bar{\mathbf{R}}^{k+1}\|_2^2 \end{aligned} \quad (39)$$

In the following, the right hand side of (39) is no less than 0, and thus the sequence $\{v_1 \|\bar{\mathbf{m}}^k\|_2^2 + v_2 \|\bar{\mathbf{n}}^k\|_2^2\}$ monotonically decreases. According to the inequality of (37), $(\mathbf{R}^*, \mathbf{d}^*, \mathbf{h}^*)$ is characterized by

$$\begin{aligned} & v_1 \langle \text{div} \cdot \mathbf{m}^*, \mathbf{R} - \mathbf{R}^* \rangle - v_1 \langle \text{div} \cdot (\nabla \mathbf{R}^* - \mathbf{d}^*), \mathbf{R} - \mathbf{R}^* \rangle \\ & - v_2 \langle \Delta \cdot \mathbf{n}^*, \mathbf{R} - \mathbf{R}^* \rangle + v_2 \langle \Delta \cdot (\Delta \mathbf{R}^* - \mathbf{h}^*), \mathbf{R} - \mathbf{R}^* \rangle \end{aligned} \quad (40)$$

$$+ \langle \mathbf{I} \cdot (\mathbf{I} \cdot \mathbf{R}^* - \mathbf{L}), \mathbf{R} - \mathbf{R}^* \rangle \geq 0$$

$$\|\mathbf{d}\|_1 - \|\mathbf{d}^*\|_1 + \langle \mathbf{m}^*, \mathbf{d} - \mathbf{d}^* \rangle + \langle \mathbf{d}^* - \nabla \mathbf{R}^*, \mathbf{d} - \mathbf{d}^* \rangle \geq 0 \quad (41)$$

$$\|\mathbf{h}\|_1 - \|\mathbf{h}^*\|_1 + \langle \mathbf{n}^*, \mathbf{h} - \mathbf{h}^* \rangle + \langle \mathbf{h}^* - \Delta \mathbf{R}^*, \mathbf{h} - \mathbf{h}^* \rangle \geq 0 \quad (42)$$

where div denotes the divergence operator. Similarly, $(\mathbf{R}^{k+1}, \mathbf{d}^{k+1}, \mathbf{h}^{k+1})$ is characterized by

$$\begin{aligned} & v_1 \langle \text{div} \cdot \mathbf{m}^k, \mathbf{R} - \mathbf{R}^{k+1} \rangle - v_1 \langle \text{div} \cdot (\nabla \mathbf{R}^{k+1} - \mathbf{d}^{k+1}), \mathbf{R} - \mathbf{R}^{k+1} \rangle \\ & - v_2 \langle \Delta \cdot \mathbf{n}^k, \mathbf{R} - \mathbf{R}^{k+1} \rangle + v_2 \langle \Delta \cdot (\Delta \mathbf{R}^{k+1} - \mathbf{h}^{k+1}), \mathbf{R} - \mathbf{R}^{k+1} \rangle \end{aligned} \quad (43)$$

$$+ \langle \mathbf{I} \cdot (\mathbf{I} \cdot \mathbf{R}^{k+1} - \mathbf{L}), \mathbf{R} - \mathbf{R}^{k+1} \rangle \geq 0$$

$$\begin{aligned} & \|\mathbf{d}\|_1 - \|\mathbf{d}^{k+1}\|_1 + \langle \mathbf{m}^k, \mathbf{d} - \mathbf{d}^{k+1} \rangle \\ & + \langle \mathbf{d}^{k+1} - \nabla \mathbf{R}^{k+1}, \mathbf{d} - \mathbf{d}^{k+1} \rangle \geq 0 \end{aligned} \quad (44)$$

$$\begin{aligned} & \|\mathbf{h}\|_1 - \|\mathbf{h}^{k+1}\|_1 + \langle \mathbf{n}^k, \mathbf{h} - \mathbf{h}^{k+1} \rangle \\ & + \langle \mathbf{h}^{k+1} - \Delta \mathbf{R}^{k+1}, \mathbf{h} - \mathbf{h}^{k+1} \rangle \geq 0 \end{aligned} \quad (45)$$

Since $(\mathbf{R}^{k+1}, \mathbf{d}^{k+1}, \mathbf{h}^{k+1})$ is the solution of (34). Then $\mathbf{R} = \mathbf{R}^{k+1}$ in (40), $\mathbf{R} = \mathbf{R}^*$ in (43), $\mathbf{d} = \mathbf{d}^{k+1}$ in (41), $\mathbf{d} = \mathbf{d}^*$ in (44), $\mathbf{h} = \mathbf{h}^{k+1}$ in (42), and $\mathbf{h} = \mathbf{h}^*$ in (45) are taken respectively. Taking addition (40) + (43) + $v_1[(41) + (44)] + v_2[(42) + (45)]$, it is derived that

$$\begin{aligned} & -v_1 \langle \bar{\mathbf{m}}^k, \bar{\mathbf{d}}^{k+1} - \nabla \bar{\mathbf{R}}^{k+1} \rangle - v_2 \langle \bar{\mathbf{n}}^k, \bar{\mathbf{h}}^{k+1} - \Delta \bar{\mathbf{R}}^{k+1} \rangle \\ & \geq v_1 \|\bar{\mathbf{d}}^{k+1} - \nabla \bar{\mathbf{R}}^{k+1}\|_2^2 + v_2 \|\bar{\mathbf{h}}^{k+1} - \Delta \bar{\mathbf{R}}^{k+1}\|_2^2 + \|\mathbf{I} \cdot \bar{\mathbf{R}}^{k+1}\|_2^2 \end{aligned} \quad (46)$$

From (39) and (46), it is deduced that

$$\begin{aligned} & (v_1 \|\bar{\mathbf{m}}^k\|_2^2 + v_2 \|\bar{\mathbf{n}}^k\|_2^2) - (v_1 \|\bar{\mathbf{m}}^{k+1}\|_2^2 + v_2 \|\bar{\mathbf{n}}^{k+1}\|_2^2) \\ & \geq v_1 \|\bar{\mathbf{d}}^{k+1} - \nabla \bar{\mathbf{R}}^{k+1}\|_2^2 + v_2 \|\bar{\mathbf{h}}^{k+1} - \Delta \bar{\mathbf{R}}^{k+1}\|_2^2 + \|\mathbf{I} \cdot \bar{\mathbf{R}}^{k+1}\|_2^2 \end{aligned} \quad (47)$$

which indicates

$$\left\{ \begin{array}{l} \{\bar{\mathbf{m}}^k : \forall k\} \text{ and } \{\bar{\mathbf{n}}^k : \forall k\} \text{ are bounded} \\ \lim_{k \rightarrow \infty} \|\bar{\mathbf{d}}^{k+1} - \nabla \bar{\mathbf{R}}^{k+1}\|_2 = 0 \\ \lim_{k \rightarrow \infty} \|\bar{\mathbf{h}}^{k+1} - \Delta \bar{\mathbf{R}}^{k+1}\|_2 = 0 \\ \lim_{k \rightarrow \infty} \|\mathbf{I} \cdot \bar{\mathbf{R}}^{k+1}\|_2 = 0 \end{array} \right. \quad (48)$$

According to the definitions of $\bar{\mathbf{R}}^k, \bar{\mathbf{d}}^k, \bar{\mathbf{h}}^k, \bar{\mathbf{m}}^k, \bar{\mathbf{n}}^k$, and together with $\mathbf{d}^* = \nabla \mathbf{R}^*$, $\mathbf{h}^* = \Delta \mathbf{R}^*$, it is drawn that

$$\left\{ \begin{array}{l} \{\mathbf{m}^k : \forall k\} \text{ and } \{\mathbf{n}^k : \forall k\} \text{ are bounded} \\ \lim_{k \rightarrow \infty} \|\mathbf{d}^{k+1} - \nabla \mathbf{R}^{k+1}\|_2 = 0 \\ \lim_{k \rightarrow \infty} \|\mathbf{h}^{k+1} - \Delta \mathbf{R}^{k+1}\|_2 = 0 \\ \lim_{k \rightarrow \infty} \|\mathbf{I} \cdot (\mathbf{R}^{k+1} - \mathbf{R}^*)\|_2 = 0 \end{array} \right. \quad (49)$$

Meanwhile, the second inequality of (37) implies

$$\begin{aligned} & v_1 \|\mathbf{d}^*\|_1 + v_2 \|\mathbf{h}^*\|_1 + \|\mathbf{I} \cdot \mathbf{R}^* - \mathbf{L}\|_2^2 \\ & \leq v_1 \|\mathbf{d}^{k+1}\|_1 + v_2 \|\mathbf{h}^{k+1}\|_1 + v_1 \langle \mathbf{m}^*, \mathbf{d}^{k+1} - \nabla \mathbf{R}^{k+1} \rangle \\ & \quad + v_2 \langle \mathbf{n}^*, \mathbf{h}^{k+1} - \Delta \mathbf{R}^{k+1} \rangle + v_1 \|\mathbf{d}^{k+1} - \nabla \mathbf{R}^{k+1}\|_2^2 \\ & \quad + v_2 \|\mathbf{h}^{k+1} - \Delta \mathbf{R}^{k+1}\|_2^2 + \|\mathbf{I} \cdot \mathbf{R}^{k+1} - \mathbf{L}\|_2^2 \end{aligned} \quad (50)$$

If $\mathbf{R} = \mathbf{R}^*$ in (43), $\mathbf{d} = \mathbf{d}^*$ in (44), and $\mathbf{h} = \mathbf{h}^*$ in (45) are taken, it is derived that

$$\begin{aligned} & v_1 \|\mathbf{d}^*\|_1 + v_2 \|\mathbf{h}^*\|_1 + \|\mathbf{I} \cdot \mathbf{R}^* - \mathbf{L}\|_2^2 \\ & \geq v_1 \|\mathbf{d}^{k+1}\|_1 + v_2 \|\mathbf{h}^{k+1}\|_1 + v_1 \langle \mathbf{m}^k, \mathbf{d}^{k+1} - \nabla \mathbf{R}^{k+1} \rangle \\ & \quad + v_2 \langle \mathbf{n}^k, \mathbf{h}^{k+1} - \Delta \mathbf{R}^{k+1} \rangle + v_1 \|\mathbf{d}^{k+1} - \nabla \mathbf{R}^{k+1}\|_2^2 \\ & \quad + v_2 \|\mathbf{h}^{k+1} - \Delta \mathbf{R}^{k+1}\|_2^2 + \|\mathbf{I} \cdot \mathbf{R}^{k+1} - \mathbf{L}\|_2^2 \end{aligned} \quad (51)$$

Together with (49), thus

$$\begin{aligned} & \liminf(v_1 \|\mathbf{d}^{k+1}\|_1 + v_2 \|\mathbf{h}^{k+1}\|_1 + \|\mathbf{I} \cdot \mathbf{R}^{k+1} - \mathbf{L}\|_2^2) \\ & \geq v_1 \|\mathbf{d}^*\|_1 + v_2 \|\mathbf{h}^*\|_1 + \|\mathbf{I} \cdot \mathbf{R}^* - \mathbf{L}\|_2^2 \\ & \geq \limsup(v_1 \|\mathbf{d}^{k+1}\|_1 + v_2 \|\mathbf{h}^{k+1}\|_1 + \|\mathbf{I} \cdot \mathbf{R}^{k+1} - \mathbf{L}\|_2^2) \end{aligned} \quad (52)$$

With taking \liminf in (50) and \limsup in (51), the proof of (35) is completed. And (35) implies that $\{\mathbf{R}^k\}$ is a minimizing sequence of $E_1(\cdot)$. If the minimizer of $E_1(\cdot)$ is unique, then $\mathbf{R}^k \rightarrow \mathbf{R}^*$.

Theorem 3. Assume $(\mathbf{R}^*, \mathbf{d}^*, \mathbf{h}^*; \mathbf{m}^*, \mathbf{n}^*)$ be a saddle point of $L(\mathbf{R}, \mathbf{d}, \mathbf{h}; \mathbf{m}, \mathbf{n})$. Suppose that the problem (34) is roughly solved in each iteration, i.e. $T = 1$ in Algorithm 1. Then the sequence $(\mathbf{R}^k, \mathbf{d}^k, \mathbf{h}^k; \mathbf{m}^k, \mathbf{n}^k)$ satisfies

$$\left\{ \begin{array}{l} \lim_{k \rightarrow \infty} v_1 \|\mathbf{d}^k\|_1 + v_2 \|\mathbf{h}^k\|_1 + \|\mathbf{I} \cdot \mathbf{R}^k - \mathbf{L}\|_2^2 = E_1(\mathbf{R}^*) \\ \lim_{k \rightarrow \infty} \|\mathbf{d}^k - \nabla \mathbf{R}^k\|_2 = 0 \\ \lim_{k \rightarrow \infty} \|\mathbf{h}^k - \Delta \mathbf{R}^k\|_2 = 0 \\ \lim_{k \rightarrow \infty} \|\mathbf{I} \cdot (\mathbf{R}^k - \mathbf{R}^*)\|_2 = 0 \end{array} \right. \quad (53)$$

And (53) indicates that $\{\mathbf{R}^k\}$ is a minimizing sequence of $E_1(\cdot)$. If the minimizer of $E_1(\cdot)$ is unique, then $\mathbf{R}^k \rightarrow \mathbf{R}^*$.

Similar to the proof for **Theorem 2**, the proof for Theorem 4.3 in Wu and Tai (2011) can also be adopted to prove **Theorem 3**, and more related details for interest readers can refer to Wu and Tai (2011).

References

- Ancuti, C.O., Ancuti, C., Haber, T., Bekaert, P., 2011. Fusion-based restoration of the underwater images. In: Proc. IEEE Intl. Conf. Image Process. pp. 1557–1560.
- Ancuti, C., Ancuti, C.O., Haber, T., Bekaert, P., 2012. Enhancing underwater images and videos by fusion. In: Proc. IEEE Conf. Comput. Vision Pattern Recognit. pp. 81–88.
- Ancuti, C.O., Ancuti, C., Vleeschouwer, C.D., Bekaert, P., 2018. Color balance and fusion for underwater image enhancement. *IEEE Trans. Image Process.* 27 (1), 379–393.
- Berman, D., Treibitz, T., Avidan, S., 2016. Non-local image dehazing. In: Proc. IEEE Conf. Comput. Vision Pattern Recognit. pp. 1674–1682.
- Boyd, S., Parikh, N., Chu, E., Peleato, B., Eckstein, J., 2011. Distributed optimization and statistical learning via the alternating direction method of multipliers. *Found. Trends Mach. Learn.* 3 (1), 1–122.
- Buchsbaum, G., 1980. A spatial processor model for object colour perception. *J. Franklin Inst.* 310 (1), 1–26.
- Cai, B., Xu, X., Jia, K., Qing, C., Tao, D., 2016. DehazeNet: An end-to-end system for single image haze removal. *IEEE Trans. Image Process.* 25 (11), 5187–5198.
- Chan, T., Esedoglu, S., Park, F., Yip, A., 2005. Recent developments in total variation image restoration. *Math. Models Comput. Vis.* 17 (2).
- Chan, R.H., Liang, H., Wei, S., Nikolova, M., Tai, X.C., 2015. High-order total variation regularization approach for axially symmetric object tomography from a single radiograph. *Inverse Probl. Imag.* 9 (1).
- Chiang, J.Y., Chen, Y.C., 2012. Underwater image enhancement by wavelength compensation and dehazing. *IEEE Trans. Image Process.* 21 (4), 1756–1769.
- Dong, C., Loy, C.C., He, K., Tang, X., 2015. Image super-resolution using deep convolutional networks. *IEEE Trans. Pattern Anal. Mach. Intell.* 38 (2), 295–307.
- Drews, P.L., Nascimento, E.R., Botelho, S.S., Campos, M.F.M., 2016. Underwater depth estimation and image restoration based on single images. *IEEE Comput. Graph. Appl.* 36 (2), 24–35.
- Ebner, M., 2007. *Color Constancy*, first ed. Wiley.
- Fabbri, C., Islam, M.J., Sattar, J., 2018. Enhancing underwater imagery using generative adversarial networks. In: Proc. IEEE Intl. Conf. Robot. Auto. pp. 7159–7165.
- Fang, S., Deng, R., Cao, Y., Fang, C., 2013. Effective single underwater image enhancement by fusion. *J. Comput.* 8 (4), 904–911.
- Farhadifard, F., Zhou, Z., von Lukas, U.F., 2015. Learning-based underwater image enhancement with adaptive color mapping. In: Proc. IEEE International Symposium on Image and Signal Processing and Analysis, pp. 48–53.
- Finlayson, G.D., Trezzi, E., 2004. Shades of gray and colour constancy. In: Proc. Color Imag. Conf. Color Sci. Syst. Appl. Soc. Imag. Sci. Technol. pp. 37–41.
- Fu, X., Fan, Z., Ling, M., Huang, Y., Ding, X., 2017. Two-step approach for single underwater image enhancement. In: Proc. International Symposium on Intelligent Signal Processing and Communication Systems, pp. 789–794.
- Fu, X., Liao, Y., Zeng, D., Huang, Y., Zhang, X.P., Ding, X., 2015. A probabilistic method for image enhancement with simultaneous illumination and reflectance estimation. *IEEE Trans. Image Process.* 24 (12), 4965–4977.
- Fu, X., Zhuang, P., Huang, Y., Liao, Y., Zhang, X.P., Ding, X., 2014. A retinex-based enhancing approach for single underwater image. In: Proc. IEEE Intl. Conf. Image Process. pp. 4572–4576.
- Galdran, A., Pardo, D., Picn, A., Alvarez-Gila, A., 2015. Automatic red-channel underwater image restoration. *J. Vis. Communun. Image Represent.* 26, 132–145.
- Goldstein, T., Osher, S., 2009. The split Bregman method for L1-regularized problems. *SIAM J. Imag. Sci.* 2 (2), 323–343.
- Goodfellow, I., et al., 2014. Generative adversarial nets. In: Proc. Advances in Neural Information Processing Systems, pp. 2672–2680.
- Grasmair, M., Lenzen, F., 2010. Anisotropic total variation filtering. *Appl. Math. Optim.* 62 (3), 323–339.
- Gu, K., Lin, W., Zhai, G., Yang, X., Zhang, W., Chen, C.W., 2017. No-reference quality metric of contrast distorted images based on information maximization. *IEEE Trans. Cybern.* 47 (12), 4559–4565.
- Guo, Y., Li, H., Zhuang, P., 2020. Underwater image enhancement using a multiscale dense generative adversarial network. *IEEE J. Ocean. Eng.* 45 (3), 862–870.
- Hautiere, N., Tarel, J.P., Aubert, D., Dumont, E., 2011. Blind contrast enhancement assessment by gradient ratioing at visible edges. *Image Anal. Stereol.* 27 (2), 87–95.
- He, K., Sun, J., Tang, X., 2011. Single image haze removal using dark channel prior. *IEEE Trans. Pattern Anal. Mach. Intell.* 33 (12), 2341–2353.
- Hiriart-Urruty, J.B., Lemarechal, C., 1996. *Convex Analysis and Minimization Algorithms*. Springer-Verlag Berlin, I.
- Hitam, M.S., Awalludin, E.A., Yussof, W.N., Bachok, Z., 2013. Mixture contrast limited adaptive histogram equalization for underwater image enhancement. In: Proc. International Conference on Computer Applications Technology, pp. 1–5.
- Iqbal, K., Abdul Salam, R., Osman, M., Talib, A.Z., 2007. Underwater image enhancement using an integrated colour model. *IAENG Int. J. Comput. Sci.* 32 (2), 239–244.
- Isola, P., Zhu, J., Zhou, T., Efros, A.A., 2017. Image-to-image translation with conditional adversarial networks. In: Proc. IEEE Conf. Comput. Vision Pattern Recognit. pp. 1125–1134.
- Jobson, D.J., Rahman, Z.U., Woodell, G.A., 1997. Properties and performance of a center/surround retinex. *IEEE Trans. Image Process.* 6 (3), 451–462.
- Khatir, S., Tiachacht, S., Thanh, C.L., Bui, T.Q., Wahab, M.A., 2019a. Damage assessment in composite laminates using ANN-PSO-IGA and Cornwell indicator. *Compos. Struct.* 230, 111509.
- Khatir, S., Wahab, M.A., 2019. Fast simulations for solving fracture mechanics inverse problems using POD-RBF XIGA and Jaya algorithm. *Eng. Fract. Mech.* 205, 285–300.
- Khatir, S., Wahab, M.A., Bouchicha, D., Khatir, T., 2019b. Structural health monitoring using modal strain energy damage indicator coupled with teaching-learning-based optimization algorithm and isogeometric analysis. *J. Sound Vib.* 448, 230–246.
- Kimmel, R., Elad, M., Shaked, D., Keshet, R., Sobel, I., 2003. A variational framework for Retinex. *Int. J. Comput. Vis.* 52 (1), 7–23.
- Land, E.H., 1964. The retinex. *Am. Sci.* 52 (2), 247–264.
- Land, E.H., 1977. The Retinex theory of color vision. *Sci. Amer.* 237 (6), 108–128.
- Land, E.H., McCann, J.J., 1971. Lightness and retinex theory. *J. Opt. Soc. Amer.* 61 (1), 1–11.
- LeCun, Y., Bengio, Y., Hinton, G., 2015. Deep learning. *Nature* 521 (7553), 436.
- Lei, T., Jia, X., Zhang, Y., Liu, S., Meng, H., 2019. Superpixel-based fast fuzzy C-means clustering for color image segmentation. *IEEE Trans. Fuzzy Syst.* 27 (9), 1753–1766.
- Li, C., Anwar, S., Poriklid, F., 2020. Underwater scene prior inspired deep underwater image and video enhancement. *Pattern Recognit.* 98, 1204–1211.
- Li, C., Guo, J., Cong, R., Pang, Y., Wang, B., 2016a. Underwater image enhancement by dehazing with minimum information loss and histogram distribution prior. *IEEE Trans. Image Process.* 25 (12), 5664–5677.
- Li, C., Guo, J., Guo, C., 2018a. Emerging from water: Underwater image color correction based on weakly supervised color transfer. *IEEE Signal Process. Lett.* 25 (3), 323–327.
- Li, C., Guo, J., Guo, C., Cong, R., Gong, J., 2017. A hybrid method for underwater image correction. *Pattern Recognit. Lett.* 94, 62–67.
- Li, C., Guo, C., Ren, W., Cong, R., Hou, J., Kwong, S., Tao, D., 2019. An underwater image enhancement benchmark dataset and beyond. *IEEE Trans. Image Process.* 29, 4376–4389.
- Li, M., Liu, J., Yang, W., Sun, X., Guo, Z., 2016b. Structure-revealing low-light image enhancement via robust retinex model. *IEEE Trans. Image Process.* 27 (6), 2828–2841.
- Li, J., Skinner, K.A., Eustice, R.M., Johnson-Roberson, M., 2018b. WaterGAN: Unsupervised generative network to enable real-time color correction of monocular underwater images. *IEEE Robot. Autom. Lett.* 3 (1), 387–394.
- Liu, H., Xu, J., Wu, Y., Guo, Q., Ibragimov, B., Xing, L., 2018. Learning deconvolutional deep neural network for high resolution medical image reconstruction. *Inform. Sci.* 468, 142–154.
- Liu, X., Zhang, H., Cheung, Y.M., You, X., Tang, Y.Y., 2017. Efficient single image dehazing and denoising: An efficient multi-scale correlated wavelet approach. *Comput. Vis. Image Und.* 162, 23–33.
- Lowe, D.G., 2004. Distinctive image features from scale-invariant keypoints. *Int. J. Comput. Vis.* 60 (2), 91–110.
- Narasimhan, S.G., Nayar, S.K., 2003. Contrast restoration of weather degraded images. *IEEE Trans. Pattern Anal. Mach. Intell.* 25 (6), 713–724.
- Ng, M.K., Wang, W., 2011. A total variation model for Retinex. *SIAM J. Imag. Sci.* 4 (1), 345–365.
- Nguyen, D.H., Bui, T.T., De Roeck, G., Wahab, M.A., 2019. Damage detection in Ca-Non Bridge using transmissibility and artificial neural networks. *Struct. Eng. Mech.* 71 (2), 175–183.
- Osher, S., Burger, M., Goldfarb, D., Xu, J., Yin, W., 2005. An iterative regularization method for total variation-based image restoration. *Multiscale Model. Simul.* 4 (2), 460–489.
- Panetta, K., Gao, C., Agaian, S., 2015. Human-visual-system-inspired underwater image quality measures. *IEEE J. Ocean. Eng.* 41 (3), 1–11.
- Peng, Y.T., Cao, K., Cosman, P.C., 2018. Generalization of the dark channel prior for single image restoration. *IEEE Trans. Image Process.* 27 (6), 2856–2868.
- Peng, Y.T., Cosman, P.C., 2017. Underwater image restoration based on image blurriness and light absorption. *IEEE Trans. Image Process.* 26 (4), 1579–1594.
- Rahman, Z.U., Jobson, D.J., Woodell, G.A., 2004. Retinex processing for automatic image enhancement. *J. Electron. Imag.* 13 (1), 100–110.
- Raimondo, S., Silvia, C., 2010. Underwater image processing: state of the art of restoration and image enhancement method. *EURASIP J. Adv. Signal Process.* 1, 1–14.
- Sattar, J., Dudek, G., 2006. On the performance of color tracking algorithms for underwater robots under varying lighting and visibility. In: Proc. IEEE International Conference on Robotics and Automation, pp. 3550–3555.
- Sattar, J., Giguere, P., Dudek, G., Prahacs, C., 2005. A visual servoing system for an aquatic swimming robot. In: Proc. IEEE/RSJ Int. Conf. Intelligent Robots and Systems, pp. 2071–2076.
- Schechner, Y.Y., Averbuch, Y., 2007. Regularized image recovery in scattering media. *IEEE Trans. Pattern Anal. Mach. Intell.* 29 (9), 1655–1660.
- Tarel, J.P., Hautiere, N., 2009. Fast visibility restoration from a single color or gray level image. In: Proc. IEEE Int. Conf. Comput. Vis. pp. 2201–2208.

- Tiachacht, S., Bouazzouni, A., Khatir, S., Wahab, M.A., Behtani, A., Capozucca, R., 2018. Damage assessment in structures using combination of a modified Cornwell indicator and genetic algorithm. *Eng. Struct.* 177, 421–430.
- Tran-Ngoc, H., Khatir, S., De Roeck, G., Bui-Tien, T., Nguyen-Ngoc, L., Wahab, M.A., 2018. Model updating for Nam O bridge using particle swarm optimization algorithm and genetic algorithm. *Sensors* 18 (12), 4131.
- Tran-Ngoc, H., Khatir, S., De Roeck, G., Bui-Tien, T., Wahab, M.A., 2019. An efficient artificial neural network for damage detection in bridges and beam-like structures by improving training parameters using cuckoo search algorithm. *Eng. Struct.* 199, 109637.
- van de Weijer, J., Gevers, T., Gijsenij, A., 2007. Edge-based color constancy. *IEEE Trans. Image Process.* 16 (9), 2207–2214.
- Vasamsetti, S., Mittal, N., Neelapu, B.C., Sardana, H.K., 2017. Wavelet based perspective on variational enhancement technique for underwater imagery. *Ocean Eng.* 141, 88–100.
- Wang, Y., Li, N., Li, Z., Gu, Z., Zheng, H., Zheng, B., Sun, M., 2018. An imaging-inspired no-reference underwater color image quality assessment metric. *Comput. Electr. Eng.* 70, 904–913.
- Wang, S., Wang, H., Zhou, Y., Liu, J., Dai, P., Du, X., Wahab, M.A., 2021. Automatic laser profile recognition and fast tracking for structured light measurement using deep learning and template matching. *Measurement* 169, 108362.
- Wen, H., Tian, Y., Huang, T., Gao, W., 2013. Single underwater image enhancement with a new optical model. In: Proc. IEEE International Symposium on Circuits and Systems, pp. 753–756.
- Wu, C.L., Tai, X.C., 2010. Augmented Lagrangian method, dual methods, and split bregman iteration for ROF, vectorial TV, and high order models. *SIAM J. Imag. Sci.* 3 (3), 300–339.
- Wu, C.L., Tai, X.C., 2011. Augmented lagrangian method for total variation restoration with non-quadratic fidelity. *Inverse Probl. Imag.* 5 (1), 237–261.
- Xu, L., Jia, J., 2010. Two-phase kernel estimation for robust motion deblurring. In: Proc. Eur. Conf. Comput. Vis. pp. 157–170.
- Yang, M., Sowmya, A., 2015. An underwater color image quality evaluation metric. *IEEE Trans. Image Process.* 24 (12), 6062–6071.
- Yang, C., Zhang, L., Lu, H., Ruan, X., Yang, M.H., 2013. Saliency detection via graph-based manifold ranking. In: Proc. IEEE Conf. Comput. Vision Pattern Recognit. pp. 3166–3173.
- Yue, H., Yang, J., Sun, X., Wu, F., Hou, C., 2017. Contrast enhancement based on intrinsic image decomposition. *IEEE Trans. Image Process.* 26 (8), 3981–3994.
- Zhu, J., Park, T., Isola, P., Efros, A.A., 2012. Unpaired image-to-image translation using cycle-consistent adversarial networks. In: Proc. IEEE Conf. Comput. Vision Pattern Recognit. pp. 81–88.
- Zhuang, P., Ding, X., 2020. Underwater image enhancement using an edge-preserving filtering retinex algorithm. *Multimedia Tools Appl.* 79, 17257–17277.